



Thesis Title

Israel Melo Sother

Thesis to obtain the Master of Science Degree in
Electrical and Computer Engineering

Supervisor(s): Prof. Full Name 1
Dr. Full Name 2

Examination Committee

Chairperson: Prof. Full Name
Supervisor: Prof. Full Name 1 (or 2)
Member of the Committee: Prof. Full Name 3

June 2024

Dedicated to someone special...

Declaration

I declare that this document is an original work of my own authorship and that it fulfills all the requirements of the Code of Conduct and Good Practices of the Universidade de Lisboa.

Acknowledgments

A few words about the university, financial support, research advisor, dissertation readers, faculty or other professors, lab mates, other friends and family...

Resumo

Inserir o resumo em Português aqui com o máximo de 250 palavras e acompanhado de 4 a 6 palavras-chave...

Palavras-chave: palavra-chave1, palavra-chave2,...

Abstract

Insert your abstract here with a maximum of 250 words, followed by 4 to 6 keywords...

Keywords: keyword1, keyword2,...

Contents

Acknowledgments	iv
Resumo	v
Abstract	vi
List of Tables	ix
List of Figures	x
Nomenclature	xii
Glossary	xii
1 Introduction	1
1.1 Motivation	1
1.2 Control Methods Overview	2
1.3 Objectives and Deliverables	3
1.4 Thesis Outline	3
2 Background	4
2.1 Formula Student	4
2.2 Two Level Voltage Source Inverter	6
2.2.1 Space Vector Modulation	7
2.3 PMSM model	9
2.3.1 Three-Phase model	9
2.3.2 Blondel-Park Transformation	10
2.3.3 dq0 Model	11
2.3.4 Discretization	13
2.4 Control Methods State of the Art	14
2.4.1 Field Oriented Control	14
2.4.2 Direct Torque Control	15
2.4.3 Model Predictive Control	16
3 Implementation	18
3.1 Motor characterization	18
3.1.1 Phase resistance	19
3.1.2 Flux Linkage	19

3.1.3	Inductance method 1	20
3.1.4	Inductance method 2	23
3.2	Current References	26
3.2.1	Voltage Constraint	28
3.3	Load profile	30
3.4	Proposed Control Methods	31
3.4.1	Finite Set MPC	31
3.4.2	Finite Set with Null Vector MPC	31
3.4.3	Explicit Continuous Set MPC	33
3.4.4	Implicit Continuous Set MPC	33
3.5	Horizon Extension	34
4	Implementation	36
4.1	Simulation	36
4.2	Simulation vs Bench Tests	40
Bibliography		41
A dq0 model with amplitude invariant transformation		45
B Technical Datasheets		47
B.1	AMK Motor Datasheet	48
B.2	AMK Inverter Datasheet	49

List of Tables

2.1	FST13 Powertrain Specifications	6
2.2	Space vector for a 2-level three-phase inverter	7
4.1	Control Method Current THD comparison	38
4.2	Car load parameters	39

List of Figures

1.1 FST12 Team at Formula Student Germany Competition.	2
2.1 Formula Student Germany Tracks.	5
2.2 2-Level Voltage source Inverter arrangement.	7
2.3 Space vector for a 2-level three-phase inverter.	8
2.4 Delta-wound PMSM.	9
2.5 Field Oriented Control - from Tex [28].	15
2.6 Direct Torque Control - from El Ouanjli et al. [34].	16
3.1 Flux Linkage characterization.	20
3.2 Inductance measurement setup schematic.	20
3.3 Inductance measurement setup.	21
3.4 Inductance measurement oscilloscope output.	22
3.5 L_d in function of i_d	22
3.6 Quadrature Inductance measurement alignment pulse setup.	23
3.7 L_q in function of i_q	23
3.8 Identification voltage pulses - from Stumberger et al. [41].	24
3.9 Quadrature Flux linkage @ $i_d = -5A$	24
3.10 Flux linkage with different currents on perpendicular axis.	25
3.11 Flux Linkage exponential fit.	25
3.12 Maximum Torque per Ampere curve without constraints.	27
3.13 Constrained Maximum Torque per Ampere curve at minimum, nominal, and maximum voltages.	29
3.14 FSMPC Diagram.	32
3.15 Finite Set with Null Vector MPC Diagram.	32
3.16 Explicit Continuous Set MPC Diagram.	33
3.17 Implicit Continuous Set MPC Diagram.	34
3.18 Horizon extension by one timestep.	34
3.19 Horizon Extension by control time.	35
4.1 Simulink Models, Motor and Inverter.	37
4.2 Torque step response.	37

4.3 Step with error on motor parameters.	39
4.4 Acceleration event comparison.	40

Chapter 1

Introduction

Contents

1.1 Motivation	1
1.2 Control Methods Overview	2
1.3 Objectives and Deliverables	3
1.4 Thesis Outline	3

1.1 Motivation

With the crescent regulation efforts to reduce carbon footprints, the mobility sector has pushed electric and hybrid powertrain development. This field has been a hot topic for not only hardware improvements [1] but also new software alternatives. From one side the crescent processing power available to microcontrollers has enabled the use of real-time predictive control strategies[2], while the use of wide bandgap semiconductors resulted in a great efficiency increase [3].

Formula Student is an engineering competition that challenges students to design, manufacture, and test a formula-style race car inside a given set of regulations. Similarly to the commercial field, the competition has pushed teams towards electrification, encouraging students to seek solutions that are lightweight, powerful, and efficient. The Formula Student Team of Técnico Lisboa (FST Lisboa) was funded in 2001, and since then has built 12 prototypes, from the fourth model (FST04) onward they have an electric powertrain, with the last 3 having autonomous racing mode, with the last one shown in figure 1.1.

As these new power electronics improvements are not yet readily available with the specifications needed for Formula Student prototypes, many teams started to develop their own solutions. FST Lisboa started working for a full in-house powertrain in 2017 with the motor development by Sarrico [4], and inverter development by Costa[5]. This allows not only a great learning experience but also full control over a more efficient platform, creating a system optimized for each prototype. Unfortunately, the motor prototype is not ready to be used in the car, and the inverter is missing a system able to control the currently used motors. This is the gap this work intends to fill, enabling the use of an in-house developed

inverter with the commercial motor solution.

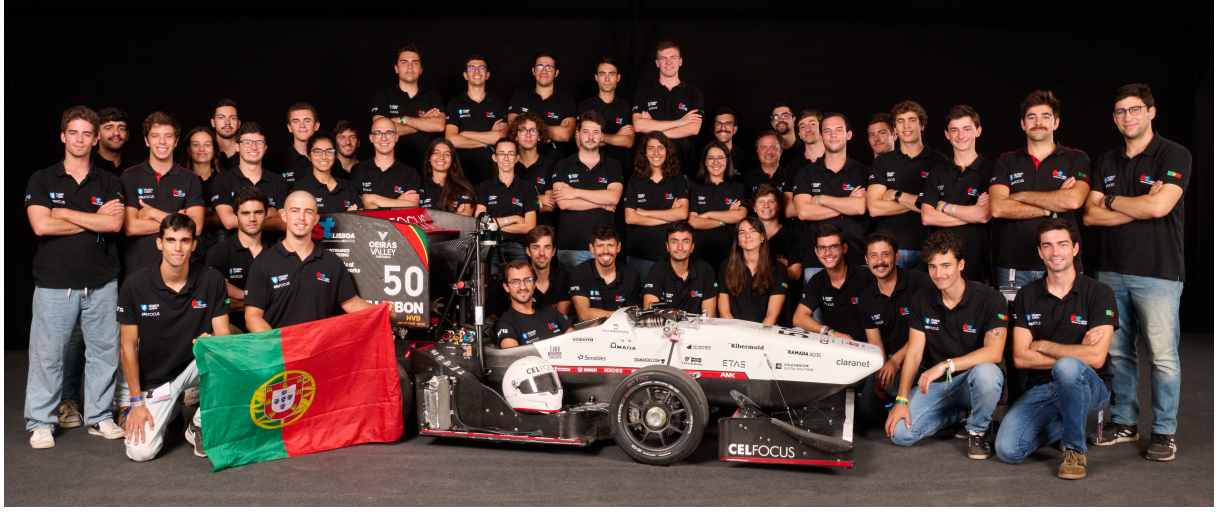


Figure 1.1: FST12 Team at Formula Student Germany Competition, © FSG - Axel Grobe.

1.2 Control Methods Overview

Through the years, several approaches have been proposed to control synchronous machines, usually, they are implemented using a 2-level three-phase inverter. Regarding the control method, several solutions have been presented in the literature as PID current control, Direct Torque Control (DTC), and Model Predictive Control (MPC)[6]. Some approaches require a modulator for the voltage applied like Space Vector Modulation (SVM)[7], while others can directly output the control signals[8].

The use of Field Oriented Control (FOC) and DTC have dominated the market for many years due to their simple implementation, but each of them has downsides. FOC combined with current PID is known for having a slow dynamic response when compared to DTC, while in steady-state behavior and disturbance rejection, it shows better results[9–11]. Another advantage of DTC strategy is that it does not need rotor position sensors, thus having a lower cost and a simpler implementation.

Technical advances in the microprocessor industry have allowed the crescent use of MPC in power converters and drives[8]. This non-linear control scheme provides easy constraint integration and fast design times while being insensitive to the type of machine being controlled, as long as the proper mathematical model is used. The main downside of this strategy is the increased computational cost, which lately has been offset by technological advances.

MPC in power systems is usually divided in two categories: Continuous Set Model Predictive Control (CS-MPC) and Finite Set Model Predictive Control (FS-MPC)[12], depending on their output signals. The first type calculates the best possible voltage vector and then uses a modulator like SVM to compose it, while FS-MPC exploits the fact that a motor drive usually has a limited number of possible voltage vectors and thus predicts the currents for each of those vectors to evaluate the best option. The second approach usually doesn't need a modulator as it only considers native vectors, although some variations have tried to increase the search space by introducing synthetic vectors that are created from a combination of the

native ones. This technique of subdivision and refining vectors can be used to create a quasi-continuous set MPC[13], which, when combined with reducing the search area to the most probable sector, can improve the torque and current ripple without a prohibitive increase in computational cost.

1.3 Objectives and Deliverables

This work targets to develop a nonlinear control strategy that allows the use of the inverter previously developed by Costa[5] with the AMK motors[14]. This control method must be able to achieve a faster dynamic response than the one from the manufacturer while maintaining the same steady-state performance, and with a sampling time smaller than $20\mu s$ to allow a switching frequency of at least 50kHz .

While the improved control method will enhance the performance, not all the gains will come from that, but also the use of an inverter with Silicon Carbide (SiC) mosfets greatly increases the efficiency. The increase in switching frequency shall bring a reduction in the currents Total Harmonic Distortion (THD) resulting in further efficiency improvements. Lastly, the use of an inverter designed specifically for this motor will reduce the system mass, improving the power-to-weight ratio.

Summing up, this work aims to increase the dynamic response and the efficiency of the powertrain system using wide bandgap semiconductors and nonlinear control methods. This will be verified with a prototype in a test bench, where multiple control methods shall be compared with the OEM system. A revised version of the inverter will also be made, to improve the measurements.

1.4 Thesis Outline

Chapter 2 starts with an overview of formula student competitions, followed by a general inverter topology. Then a mathematical model for a Permanent Magnet Synchronous Motor (PMSM) is developed, laying the ground for the proposal of the control methods.

In Chapter 3 the motor characterization methodology is defined and the current reference generation is presented.

Chapter 4 presents simulations comparing the control methods and validation of the simulation model with experimental tests.

The experimental results are shown in Chapter 5.

In Chapter 6 the conclusions are made, analyzing which objectives were fulfilled and proposing topics for future research.

Chapter 2

Background

Contents

2.1 Formula Student	4
2.2 Two Level Voltage Source Inverter	6
2.2.1 Space Vector Modulation	7
2.3 PMSM model	9
2.3.1 Three-Phase model	9
2.3.2 Blondel-Park Transformation	10
2.3.3 dq0 Model	11
2.3.4 Discretization	13
2.4 Control Methods State of the Art	14
2.4.1 Field Oriented Control	14
2.4.2 Direct Torque Control	15
2.4.3 Model Predictive Control	16

This chapter covers some fundamentals used to develop this work. It starts with a brief overview of Formula Student competitions and the current powertrain system used by FST Lisboa. After this, it presents the basics on Voltage Source Inverter (VSI) and modulation techniques before developing a mathematical model for the used motors and later converting it to discrete time. Lastly, a quick overview of the literature control methods is done before introducing the proposed strategy.

2.1 Formula Student

In a formula student competition, two types of evaluation exist, the first is static events where the design, cost, and business model of the prototype are analyzed. In the dynamic category, each prototype is evaluated through 5 different events: Skidpad, Acceleration, AutoX, Endurance, and Efficiency (evaluated in the Endurance track), as shown in figure figure 2.1. The Skidpad event is less relevant for this study as it is a steady state circle of radius 9.125m, thus being a low power course with the dynamic

response of the motors having almost no relevance on the performance. The acceleration event consists of a 75m straight with the maximum battery power limited to 80kw, as it is for all Formula Student events. For this event, the key factors are the torque dynamic response, and how efficiently the powertrain system can deliver power to the ground. The AutoX is a 1km track with several corners and straights mixed. In this test, an increased dynamic response can delay the braking zone, and the efficiency allows it to reach higher velocities using the same amount of power. Lastly, the endurance event is similar to the AutoX, with enough laps to complete 22km. In this event, although improved dynamics can be beneficial, efficiency is the key factor as it results in more available energy to complete the 22km track while also scoring points in the Efficiency category.

For the autonomous part of the competition, there are very similar events, with the Skidpad and Acceleration being the same as in the manual mode. The driverless AutoX needs to be a little different, with a smaller distance for the Autonomous System Responsible (ASR) to be able to see the car through the entire track and press the emergency button if necessary. The Endurance event driverless analogous is the TrackDrive event, usually being on the same track as the AutoX, but with fixed 10 laps. Currently, the points performance in the driverless events is mostly dictated by how good the autonomous software is, but as the teams evolve, the cars will play a major role in the results, the same way it is with the manual category.

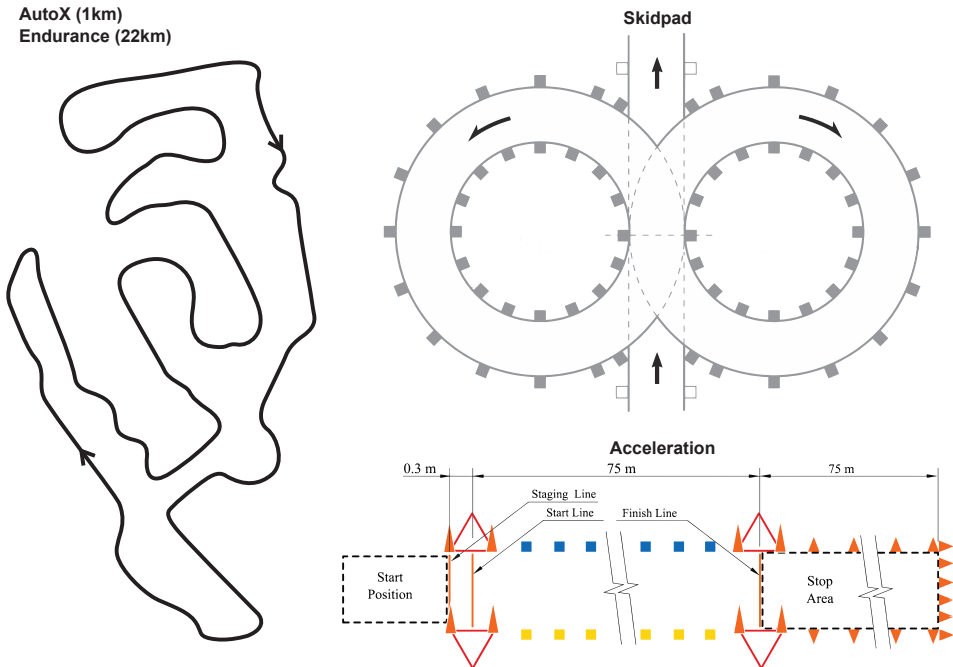


Figure 2.1: Formula Student Germany Tracks, adapted from [15].

Since the FST07, FST Lisboa has used AMK motors and inverters[14, 16], this set is a good solution for teams switching to a four-motor setup as it is already paired and has good documentation. However, as the team evolves, it is natural to look for improvements, and the AMK inverters were deemed one of the prototypes' current bottlenecks. The use of Insulated-Gate Bipolar Transistor (IGBT) as the switching component, means that this inverter is capped in its switching frequency, using only 8kHz. This low

switching frequency reduces powertrain efficiency and increases the set's weight. Another drawback of this solution is the control method as it uses a simple Field Oriented Control (FOC), thus having a low dynamic response and further reducing efficiency by not using Maximum Torque per Ampere (MTPA) strategies. A brief outline of the current specification of FST Lisboa's prototype is shown in table 2.1.

Table 2.1: FST13 Powertrain Specifications

Parameter	Value
Battery Voltage Min	420 V
Battery Voltage Maximum	609 V (limited at 600 V by regulations)
Battery Voltage Nominal	532 V
Maximum Power	147 kW (limited at 80 kW by regulations)
Number of Motors	4
Maximum Power per Motor	36.75 kW
Typical Average Power	30 kW
Maximum Average Power (1 min)	60 kW
Maximum Current DC	160 A
Maximum motor current RMS (1,24s)	105 A
AMK Inverter Switching Frequency	8 kHz
Motor Frequency at Maximum Speed	1.6 kHz
Rated Motor Current	41 Arms
Rated Motor Voltage	350 V
Maximum Speed	20000 RPM
Motor Number of Poles	10
Quadrature Axis Inductance,	0.12 mH
Direct Axis Inductance	0.24 mH
Rotor time constant	0.01 s
Maximum Torque	21 Nm
Torque constant	0.26 Nm/Arms
Voltage constant	18.8 V/kRPM

2.2 Two Level Voltage Source Inverter

The usual hardware used to control synchronous machines is a 2-level Voltage Source Inverter. Such equipment is composed of six switches, organized in three half bridges, one connected to each motor terminal, as shown in figure figure 2.2.

Usually, each switch in a half-bridge is operated with the inverse logic of the other switch in the half-bridge, and this arrangement allows for 8 different switch combinations where 2 of them result in null vectors. That gives 7 possible voltage vectors, as detailed in table 2.2 and figure 2.3.

This implementation only allows the control to apply discrete levels of voltage to each motor terminal, but using some modulation techniques it is possible to synthesize a resultant vector if it is inside the attainable region denoted by the hexagon in figure 2.3.

The current inverter used by FST Lisboa uses this structure, but the switches are IGBTs, which

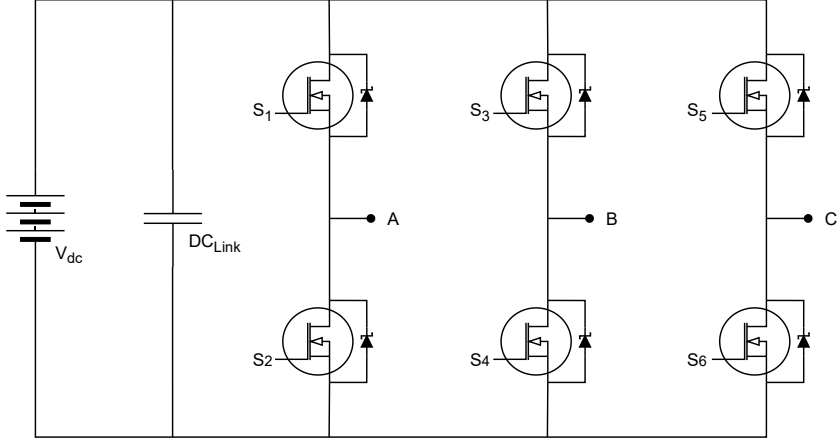


Figure 2.2: 2-Level Voltage source Inverter arrangement.

Table 2.2: Space vector for a 2-level three-phase inverter

Switch State	Vector	V_{AB}	V_{BC}	V_{CA}
0	000	0	0	0
1	001	V_{dc}	0	$-V_{dc}$
2	010	$-V_{dc}$	V_{dc}	0
3	011	0	V_{dc}	$-V_{dc}$
4	100	0	$-V_{dc}$	V_{dc}
5	101	V_{dc}	$-V_{dc}$	0
6	110	$-V_{dc}$	0	V_{dc}
7	111	0	0	0

when compared to wide bandgap semiconductors has a higher switching loss, leading to lower switching frequencies being used [17]. The lower switching frequencies cause higher distortions in the current waveforms, decreasing motor efficiency. The lower switching frequency system also needs a higher capacitance on the DC Link, while the lower efficiency of silicon semiconductors requires a bigger heatsink, leading to a higher volume and mass inverter, decreasing the power density of the solution.

2.2.1 Space Vector Modulation

Several modulation techniques have been proposed in the literature like Sinusoidal pulse-width modulation (SPWM), Selective harmonic elimination (SHE)[18], Space Vector Modulation (SVM)[7], or Space-vector control (SVC)[19]. Some of these techniques are exclusive of multilevel inverters, like SVC[20], while others also work for two-level inverters. The most common method of modulation in digital motor control is SVM, as it is a robust and easy-to-implement technique.

SVM is a simple method where to compose a given vector V_{ref} , it rapidly switches between the adjacent vectors and a null vector, so the average vector in a given time is equal to the reference vector. Suppose that the reference vector is the one shown in figure 2.3, then SVM proposes that it can be modulated by using V_1 half of the active time and V_3 on the other half of the active time. The distinction here between active and null time is regarding the used vector amplitude. To achieve vectors with an amplitude smaller than the maximum it is necessary to use null vectors, thus reducing the output amplitude. That is equivalent to equation (2.1). Where $T_1 + T_3$ is equal to the active time, and T_0 is the

null time.

$$V_{ref} = \frac{T_0 V_0 + T_1 V_1 + T_3 V_3}{h} \quad (2.1)$$

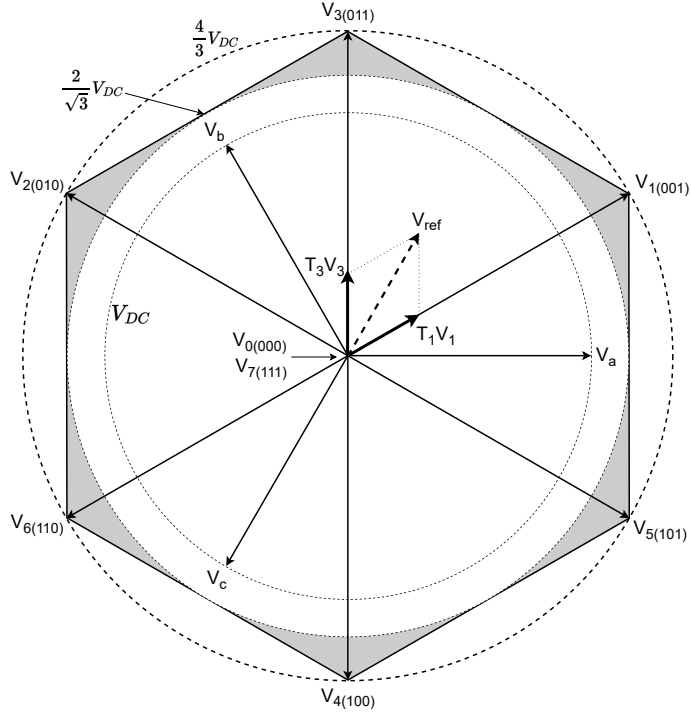


Figure 2.3: Space vector for a 2-level three-phase inverter.

Using SVM it is possible to modulate any vector inside the hexagon shown in figure 2.3, but if a clean Sinusoidal output wave is desired, the vectors should be constrained to the inscribed circle, that has a radius of $\frac{2}{\sqrt{3}}V_{DC}$. The reason behind this is to keep the reference vector locus inside the hexagon, avoiding distortions in the output. Note that although it is possible to generate waveforms with higher RMS value, it is not possible to modulate a peak higher than $\frac{2}{\sqrt{3}}V_{DC}$, thus those waveforms become more and more distorted as the amplitude approaches $\frac{4}{3}V_{DC}$ as to modulate a sinusoidal output the vector should develop a circular trajectory, but the voltage constrains it to the voltage hexagon, and thus the difference between the intended and the effectively applied vector increases.

To simplify the analysis of those vectors, a modulation index (m) is defined as shown in equation (2.2). The output is free of distortion if $m \leq \frac{2}{\sqrt{3}}$, and increasing the modulation index further will result in diminishing returns in wave amplitude, while the output approaches a six-step commutation, greatly increasing the Total Harmonic Distortion (THD)[21]. This area of operation is called overmodulation, and several approaches have been proposed[22, 23] to minimize the distortions.

$$m = \frac{|V_{ref}|}{V_{DC}} \quad (2.2)$$

2.3 PMSM model

As the proposed work is to improve the dynamic response and efficiency of the motor and motor drive currently used by FST Lisboa, it is necessary to first develop a model to represent this machine, a Permanent Magnet Synchronous Motor (PMSM) with delta-arranged windings.

2.3.1 Three-Phase model

A common way to represent the stator voltages of an electrical machine is:

$$\begin{bmatrix} u_{AB} \\ u_{BC} \\ u_{CA} \end{bmatrix} = \begin{bmatrix} r_a & 0 & 0 \\ 0 & r_b & 0 \\ 0 & 0 & r_c \end{bmatrix} \begin{bmatrix} i_a \\ i_b \\ i_c \end{bmatrix} + \frac{d}{dt} \begin{bmatrix} \psi_a \\ \psi_b \\ \psi_c \end{bmatrix} \quad (2.3)$$

In this equation, u_{xy} represents the measured voltage between terminal x and y , i_x is the current flowing on each phase, r_x is the phase resistance, and ψ_x is the flux linkage of each coil.

If the flux linkage is replaced with equation (2.4a), this can be expanded into a simpler form, shown in figure 2.4, where E_x is the back EMF as defined in equation (2.4b).

$$\psi_{abc} = \mathbf{L}_{abc} \mathbf{i}_{abc} \quad (2.4a) \quad \begin{bmatrix} E_a \\ E_b \\ E_c \end{bmatrix} = \frac{d\mathbf{L}_{abc}}{dt} \mathbf{i}_{abc} \quad (2.4b)$$

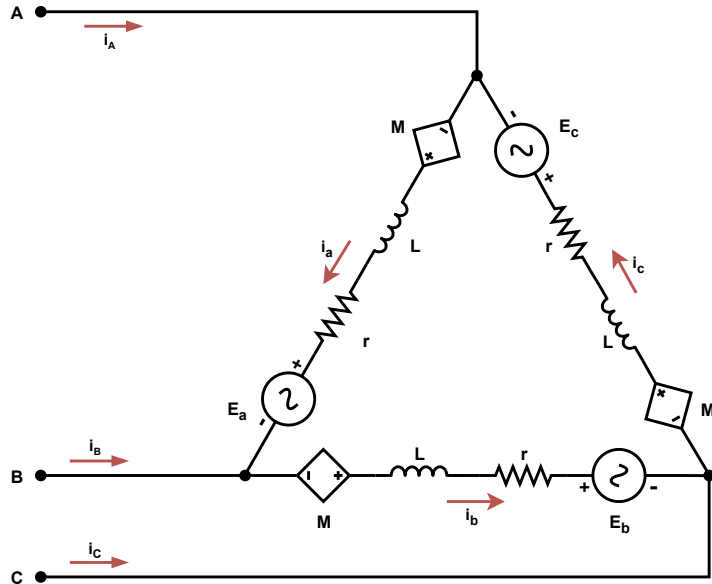


Figure 2.4: Delta-wound PMSM, modified from Pramod [24].

The expanded form results in equation (2.5).

$$u_{abc} = \mathbf{R}_{abc} \mathbf{i}_{abc} + \mathbf{L}_{abc} \frac{di_{abc}}{dt} + \frac{d\mathbf{L}_{abc}}{dt} \mathbf{i}_{abc} \quad (2.5)$$

Where \mathbf{L} is the inductance matrix, and \mathbf{r} is the resistance matrix. Note that the inductances are

not constant, but they change regarding the rotor electrical position θ_e . This variation exists because the selected machine has a spoke magnet arrangement on the rotor, thus creating magnetic paths with different resistances depending on the rotor angle. According to Marques [25], this variation is a sum of even harmonics of a cosine function, but usually, it is enough to consider up to the second one, resulting in the inductance matrix shown in equation (2.6a), where $L_{x_1}, L_{x_2}, M_{xy_1}$, and M_{xy_2} are constants and define the coefficients for the self inductances and the mutual inductances.

$$\mathbf{L}_{abc} = \begin{bmatrix} L_{a_1} + L_{a_2} \cos(2\theta_e) & M_{ab_1} + M_{ab_2} \cos(2\theta_e + \frac{4\pi}{3}) & M_{ac_1} + M_{ac_2} \cos(2\theta_e - \frac{4\pi}{3}) \\ M_{ba_1} + M_{ba_2} \cos(2\theta_e + \frac{4\pi}{3}) & L_{b_1} + L_{b_2} \cos(2\theta_e - \frac{4\pi}{3}) & M_{bc_1} + M_{bc_2} \cos(2\theta_e) \\ M_{ca_1} + M_{ca_2} \cos(2\theta_e - \frac{4\pi}{3}) & M_{cb_1} + M_{cb_2} \cos(2\theta_e) & L_{c_1} + L_{c_2} \cos(2\theta_e + \frac{4\pi}{3}) \end{bmatrix} \quad (2.6a)$$

$$\mathbf{R}_{abc} = \begin{bmatrix} r_a & 0 & 0 \\ 0 & r_b & 0 \\ 0 & 0 & r_c \end{bmatrix} \quad (2.6b)$$

Is important to explain that the equation (2.6a) is derived assuming the 3 phases are separated by 120 electrical degrees and that the coils are sinusoidally distributed.

2.3.2 Blondel-Park Transformation

The Blondel-Park transformation is a combination of the Concordia transformation, and the Park referential change, it produces a biphasic equivalent system with a synchronous rotating referential. The transformation matrix is shown in equation (2.7).

$$\mathbf{T}_{(\theta_e)} = \sqrt{\frac{2}{3}} \begin{bmatrix} 1 & 0 & \frac{1}{\sqrt{2}} \\ -\frac{1}{2} & \frac{\sqrt{3}}{2} & \frac{1}{\sqrt{2}} \\ -\frac{1}{2} & -\frac{\sqrt{3}}{2} & \frac{1}{\sqrt{2}} \end{bmatrix} \begin{bmatrix} \cos(\theta_e) & -\sin(\theta_e) & 0 \\ \sin(\theta_e) & \cos(\theta_e) & 0 \\ 0 & 0 & 1 \end{bmatrix} = \sqrt{\frac{2}{3}} \begin{bmatrix} \cos(\theta_e) & -\sin(\theta_e) & \frac{1}{\sqrt{2}} \\ \cos(\theta_e - \frac{2\pi}{3}) & -\sin(\theta_e - \frac{2\pi}{3}) & \frac{1}{\sqrt{2}} \\ \cos(\theta_e - \frac{4\pi}{3}) & -\sin(\theta_e - \frac{4\pi}{3}) & \frac{1}{\sqrt{2}} \end{bmatrix} \quad (2.7)$$

The power invariant transformation has the advantage of being an orthogonal matrix, thus $\mathbf{T}^{-1} = \mathbf{T}^T$.

If the amplitude invariant form is used, as in equation (2.8), and the orthogonality is lost.

$$\mathbf{T}_{(\theta_e)}^* = \begin{bmatrix} \cos(\theta_e) & -\sin(\theta_e) & 1 \\ \cos(\theta_e - \frac{2\pi}{3}) & -\sin(\theta_e - \frac{2\pi}{3}) & 1 \\ \cos(\theta_e - \frac{4\pi}{3}) & -\sin(\theta_e - \frac{4\pi}{3}) & 1 \end{bmatrix} \quad (2.8a)$$

$$\mathbf{T}_{(\theta_e)}^{*-1} = \frac{2}{3} \begin{bmatrix} \cos(\theta_e) & \cos(\theta_e - \frac{2\pi}{3}) & \cos(\theta_e - \frac{4\pi}{3}) \\ -\sin(\theta_e) & -\sin(\theta_e - \frac{2\pi}{3}) & -\sin(\theta_e - \frac{4\pi}{3}) \\ \frac{1}{2} & \frac{1}{2} & \frac{1}{2} \end{bmatrix} \quad (2.8b)$$

Applying the power invariant transformation to the abc variables results in:

$$\mathbf{R}_{dq0} = \mathbf{T}_{(\theta_e)}^T \mathbf{R}_{abc} \mathbf{T}_{(\theta_e)} \quad (2.9a) \qquad \mathbf{L}_{dq0} = \mathbf{T}_{(\theta_e)}^T \mathbf{L}_{abc} \mathbf{T}_{(\theta_e)} \quad (2.9b)$$

$$\mathbf{i}_{\text{abc}} = \mathbf{T}_{(\theta_e)} \mathbf{i}_{\text{dq0}} \quad (2.9\text{c})$$

$$\mathbf{u}_{\text{dq0}} = \mathbf{T}_{(\theta_e)}^T \mathbf{u}_{\text{abc}} \quad (2.9\text{d})$$

$$\boldsymbol{\psi}_{\text{abc}} = \mathbf{T}_{(\theta_e)} \boldsymbol{\psi}_{\text{dq0}} \quad (2.9\text{e})$$

2.3.3 dq0 Model

Assuming the three phases are well balanced and using the Blondel-Park transformation (power invariant form) to transform the model into a two-phase system with a rotating referential, new resistance and inductance matrixes can be calculated to this new referential. The new matrixes are shown in equation (2.10), with the subscripts $d, q, 0$, denoting the direct axis, the quadrature axis, and the zero-sequence axis, respectively. The transformation of the matrixes is detailed in Marques [25].

$$\mathbf{R}_{\text{dq0}} = \begin{bmatrix} r_a & 0 & 0 \\ 0 & r_b & 0 \\ 0 & 0 & r_c \end{bmatrix} = \begin{bmatrix} r & 0 & 0 \\ 0 & r & 0 \\ 0 & 0 & r \end{bmatrix} \quad (2.10\text{a})$$

$$\mathbf{L}_{\text{dq0}} = \begin{bmatrix} L_d & 0 & 0 \\ 0 & L_q & 0 \\ 0 & 0 & L_0 \end{bmatrix} \quad (2.10\text{b})$$

Starting with equation (2.3) and replacing the currents and flux:

$$\begin{aligned} \mathbf{u}_{\text{abc}} &= \mathbf{R}_{\text{abc}} \mathbf{T}_{(\theta_e)} \mathbf{i}_{\text{dq0}} + \frac{d(\mathbf{T}_{(\theta_e)} \boldsymbol{\psi}_{\text{dq0}})}{dt} \\ &= \mathbf{R}_{\text{abc}} \mathbf{T}_{(\theta_e)} \mathbf{i}_{\text{dq0}} + \dot{\theta}_e \frac{d\mathbf{T}_{(\theta_e)}}{d\theta_e} \boldsymbol{\psi}_{\text{dq0}} + \mathbf{T}_{(\theta_e)} \frac{d\boldsymbol{\psi}_{\text{dq0}}}{dt} \end{aligned}$$

Replacing $\dot{\theta}_e$ with ω_e , and multiplying $\mathbf{T}_{(\theta_e)}^T$ to the left results in:

$$\mathbf{u}_{\text{dq0}} = \mathbf{R}_{\text{dq0}} \mathbf{i}_{\text{dq0}} + \mathbf{T}_{(\theta_e)}^T \omega_e \frac{d\mathbf{T}_{(\theta_e)}}{d\theta_e} \boldsymbol{\psi}_{\text{dq0}} + \mathbf{T}_{(\theta_e)}^T \mathbf{T}_{(\theta_e)} \frac{d\boldsymbol{\psi}_{\text{dq0}}}{dt}$$

As the transformation matrix is orthogonal, it can be further simplified as:

$$\mathbf{u}_{\text{dq0}} = \mathbf{R}_{\text{dq0}} \mathbf{i}_{\text{dq0}} + \omega_e \mathbf{T}_{(\theta_e)}^T \frac{d\mathbf{T}_{(\theta_e)}}{d\theta_e} \boldsymbol{\psi}_{\text{dq0}} + \frac{d\boldsymbol{\psi}_{\text{dq0}}}{dt}$$

Lastly, calculate the derivative of the transformation:

$$\mathbf{T}_{(\theta_e)}^T \frac{d\mathbf{T}_{(\theta_e)}}{d\theta_e} = \frac{2}{3} \begin{bmatrix} \cos(\theta_e) & \cos(\theta_e - \frac{2\pi}{3}) & \cos(\theta_e - \frac{4\pi}{3}) \\ -\sin(\theta_e) & -\sin(\theta_e - \frac{2\pi}{3}) & -\sin(\theta_e - \frac{4\pi}{3}) \\ \frac{1}{\sqrt{2}} & \frac{1}{\sqrt{2}} & \frac{1}{\sqrt{2}} \end{bmatrix} \begin{bmatrix} -\sin(\theta_e) & -\cos(\theta_e) & 0 \\ -\sin(\theta_e - \frac{2\pi}{3}) & -\cos(\theta_e - \frac{2\pi}{3}) & 0 \\ -\sin(\theta_e - \frac{4\pi}{3}) & -\cos(\theta_e - \frac{4\pi}{3}) & 0 \end{bmatrix}$$

$$\mathbf{T}_{(\theta_e)}^T \frac{d\mathbf{T}_{(\theta_e)}}{d\theta_e} = \begin{bmatrix} 0 & -1 & 0 \\ 1 & 0 & 0 \\ 0 & 0 & 0 \end{bmatrix}$$

Thus, the PMSM model in the dq0 frame is presented in equation (2.11). This approach can be used for the amplitude invariant transformation and will result in the same form of equation (appendix A), but the equation will be scaled by a factor of $\sqrt{\frac{3}{2}}$ in the d and q axis, while the zero axis can give different

results.

$$\mathbf{u}_{dq0} = \mathbf{R}_{dq0}\mathbf{i}_{dq0} + \omega_e \begin{bmatrix} 0 & -1 & 0 \\ 1 & 0 & 0 \\ 0 & 0 & 0 \end{bmatrix} \boldsymbol{\psi}_{dq0} + \frac{d\boldsymbol{\psi}_{dq0}}{dt} \quad (2.11)$$

Is worth noticing that because this is a delta wound machine, the sum of the phase currents is not necessarily zero, and as such, it is mathematically possible to have a circulating current through the phases [24], thus the zero-sequence component is not directly zero as in a Y wound device. For such currents to exist, an external exciting winding, a relevant non-considered inductance harmonic, or an imbalance through the phases is necessary. Even when those currents are present, they are usually dependent on the rotor position, and cannot be controlled with the standard 3-terminal connection, thus for the sake of simplicity, they are discarded throughout this work, which gives equation (2.12).

$$u_d = ri_d + \frac{d\psi_d}{dt} - \omega_e \psi_q \quad (2.12a)$$

$$u_q = ri_q + \frac{d\psi_q}{dt} + \omega_e \psi_d \quad (2.12b)$$

$$T_e = p(\psi_d i_q - \psi_q i_d) \quad (2.12c)$$

$$\frac{d\omega_e}{dt} = \frac{T_e - T_{load} - T_{loss}}{J} \quad (2.12d)$$

$$\frac{d\theta_e}{dt} = \omega_e \quad (2.12e)$$

Here ω_e is the rotor electrical rotational velocity, p is the number of pole pairs, J is the rotor rotational inertia, while T_e is the electromagnetic torque, T_{load} is the reaction torque of the load attached to the motor, and T_{loss} is a torque equivalent to the losses on the motor (such as iron or friction losses).

If ψ is assumed to be of form $\psi = i_x L_x + \psi_{PM_x}$ where the inductance only varies with the current and the permanent magnets flux (ψ_{PM_x}) is defined as constant and affecting only the direct axis, equations (2.12a) and (2.12b) becomes:

$$u_d = ri_d + \frac{di_d}{dt} \left(L_d + i_d \frac{dL_d}{di_d} \right) - \omega_e L_q i_q \quad (2.13a)$$

$$u_q = ri_q + \frac{di_q}{dt} \left(L_q + i_q \frac{dL_q}{di_q} \right) + \omega_e (L_d i_d + \psi_{PM}) \quad (2.13b)$$

Note that in equation (2.13) the cross-magnetization effect is not accounted for, but the saturation is included in the inductance variation [26]. If the inductance derivative is small when compared with the other terms, it can be further simplified to:

$$u_d = ri_d + L_d \frac{di_d}{dt} - \omega_e L_q i_q \quad (2.14a)$$

$$u_q = ri_q + L_q \frac{di_q}{dt} + \omega_e (L_d i_d + \psi_{PM}) \quad (2.14b)$$

Lastly, for the sake of completeness, if the amplitude invariant Blondel-Park transformation is used, the currents need to be multiplied by a factor of $\sqrt{\frac{3}{2}}$ in the torque equation to have a power conservative output, resulting in equation (2.15). The $\sqrt{\frac{2}{3}}$ next to the ψ_{PM} is just a reminder that the flux linkage value has a different value depending on the dq0 transformation used.

$$T_e = 1.5p i_q ((L_d - L_q)i_d + \sqrt{\frac{2}{3}}\psi_{PM}) \quad (2.15)$$

2.3.4 Discretization

An approximation of the differential equations is needed to discretize the equations to be able to use the model in a discrete time control system. Two usual solutions are the Backward and the Forward Euler methods. Although simpler to compute, the Forward Euler method is less precise, and prone to instabilities when compared to the Backward alternative, especially in fast systems such as power converters. Due to those disadvantages, the Euler Backward technique will be prioritized.

From equation (2.14), knowing that the currents and voltages vary with time and that the inductances are dependant on the currents, it is possible to discretize the system with h as the sampling time, and $t = kh$:

$$\left\{ \begin{array}{l} \frac{i_{d(k+1)} - i_{d(k)}}{h} = \frac{u_{d(k+1)} - ri_{d(k+1)} + \omega_{e(k+1)}L_{q(i_q(k+1))}i_{q(k+1)}}{L_{d(i_d(k+1))}} \\ \frac{i_{q(k+1)} - i_{q(k)}}{h} = \frac{u_{q(k+1)} - ri_{q(k+1)} - \omega_{e(k+1)}(L_{d(i_d(k+1))}i_{d(k+1)} + \psi_{PM})}{L_{q(i_q(k+1))}} \\ T_{e(k+1)} = p i_{q(k+1)} ((L_{d(i_d(k+1))} - L_{q(i_q(k+1))})i_{d(k+1)} + \psi_{PM}) \\ \frac{\omega_{e(k+1)} - \omega_{e(k)}}{h} = \frac{T_{e(k+1)} - T_{load(k+1)} - T_{loss(k+1)}}{J} \\ \frac{\theta_{e(k+1)} - \theta_{e(k)}}{h} = \omega_{e(k+1)} \end{array} \right. \quad (2.16)$$

This set of equations has an algebraic loop, where the currents in $k+1$ depend on the value of $\omega_{(k+1)}$, that depends on the value of $T_{e(k+1)}$ that is defined by the currents $k+1$. The same thing happens with the inductances, as they depend on the currents, but the currents define the value of inductance. Those problems are solved by first assuming that the inductance change due to the current change in a time step is small enough so that the inductances can be calculated using the previous time step currents. Similarly, the rotor speed is assumed to vary little between iterations, so that the value of $\omega_{(k+1)}$ can be replaced by $\omega_{(k)}$.

With those considerations, and rearranging the equations:

$$\left\{ \begin{array}{l} i_{d(k+1)} = \frac{h(u_{d(k+1)} + \omega_{e(k)} L_{q(i_q(k))} i_{q(k+1)}) + i_{d(k)} L_{d(i_d(k))}}{hr + L_{d(i_d(k))}} \\ i_{q(k+1)} = \frac{h(u_{q(k+1)} - \omega_{e(k)} (L_{d(i_d(k))} i_{d(k+1)} + \psi_{PM})) + i_{q(k)} L_{q(i_q(k))}}{hr + L_{q(i_q(k))}} \\ T_{e(k+1)} = p i_{q(k+1)} ((L_{d(i_d(k+1))} - L_{q(i_q(k+1))}) i_{d(k+1)} + \psi_{PM}) \\ \omega_{e(k+1)} = \omega_{e(k)} + h \left(\frac{T_{e(k+1)} - T_{load(k+1)} - T_{loss(k+1)}}{J} \right) \\ \theta_{e(k+1)} = \theta_{e(k)} + h \omega_{e(k+1)} \end{array} \right. \quad (2.17)$$

Or, in matrix form:

$$\begin{bmatrix} i_{d(k+1)} \\ i_{q(k+1)} \end{bmatrix} = \begin{bmatrix} 1 & -h \frac{\omega_{e(k)} L_{q(i_q(k))}}{hr + L_{d(i_d(k))}} \\ h \frac{\omega_{e(k)} L_{d(i_d(k))}}{hr + L_{q(i_q(k))}} & 1 \end{bmatrix}^{-1} \left(\begin{bmatrix} \frac{L_{d(i_d(k))}}{hr + L_{d(i_d(k))}} & 0 \\ 0 & \frac{L_{q(i_q(k))}}{hr + L_{q(i_q(k))}} \end{bmatrix} \begin{bmatrix} i_{d(k)} \\ i_{q(k)} \end{bmatrix} + \begin{bmatrix} \frac{h}{hr + L_{d(i_d(k))}} & 0 \\ 0 & \frac{h}{hr + L_{q(i_q(k))}} \end{bmatrix} \begin{bmatrix} u_{d(k+1)} \\ u_{q(k+1)} \end{bmatrix} + \begin{bmatrix} 0 \\ -h \frac{\omega_{e(k)} \psi_{PM}}{hr + L_{q(i_q(k))}} \end{bmatrix} \right) \quad (2.18a)$$

$$T_{e(k+1)} = p i_{q(k+1)} ((L_{d(i_d(k+1))} - L_{q(i_q(k+1))}) i_{d(k+1)} + \psi_{PM}) \quad (2.18b)$$

$$\begin{bmatrix} \omega_{e(k+1)} \\ \theta_{e(k+1)} \end{bmatrix} = \begin{bmatrix} 1 & 0 \\ h & 1 \end{bmatrix} \begin{bmatrix} \omega_{e(k)} \\ \theta_{e(k)} \end{bmatrix} + \frac{T_{e(k+1)} - T_{load(k+1)} - T_{loss(k+1)}}{J} \begin{bmatrix} h \\ h^2 \end{bmatrix} \quad (2.18c)$$

2.4 Control Methods State of the Art

The quest for higher efficiency and performance has pushed the development in the field of control of electrical machines, and even though several advances have been made, the main strategies in the market are still the FOC with PID current control, and DTC. While robust and well-known, these methods cannot explore the full performance envelope of the controlled machines, and the development of more complex machines with increased dynamic response and efficiency has pushed for new control strategies. In this context, the use of MPC has grown as a good alternative as it explicitly considers the system dynamics and constraints.

2.4.1 Field Oriented Control

For many years field oriented control has been one of the cornerstones of electrical machine control due to its simplicity and easy implementation[27]. This technique is based on the Blondel Park transformation, where it converts the currents and voltages from a stationary ABC reference frame into a rotating referential dq0. This allows the individual control of the motor magnetic flux and torque, which are proportional to i_d and i_q respectively. These currents usually are controlled using two separated

PIDs, where the quadrature current reference comes from the desired motor torque and the direct current comes from the field weakening strategy. The PIDs compare the references with the measured values and output a voltage to be applied in each axis, voltages that are passed to a modulator (usually SVM) to calculate the duty cycle of each MOSFET and generate the control signals. An example of such a system is shown in figure 2.5.

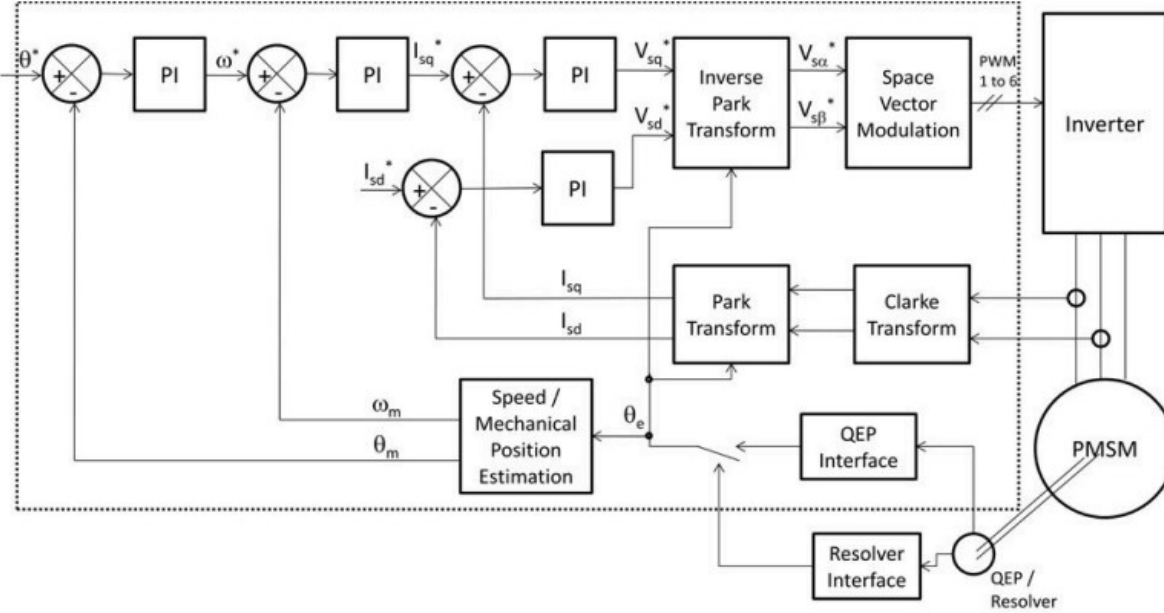


Figure 2.5: Field Oriented Control - from Tex [28].

While simple and robust, this technique heavily depends on the rotor position which is not always available, thus often needing some form of estimation to work correctly. Despite this limitation, FOC is a versatile method, being suitable not only for PMSM, but also for induction motors, reluctance machines, among others[29, 30]. One of the great advantages of FOC is that it produces a smooth operation in the full range of the motor, with low current distortions and reduced torque ripple[31].

2.4.2 Direct Torque Control

The principal rival of FOC is DTC, it shows better dynamic response with simpler implementation and less dependency on machine characterization[29]. Popularized by its use on induction machines, this method usually operates at the abc reference frame, calculating the flux based on the voltage and current vectors as in equation (2.19a), where V_s is the stator voltage vector, I_s is the stator current vector, R_s is the stator resistance matrix, and ψ_r is the rotor magnetic flux vector. Using this information, the torque can be calculated as in equation (2.19b), where p is the number of pole pairs. When using an induction machine it is not necessary to have a rotor position, but on PMSM this becomes a necessity as in FOC.

$$\psi_s = \int (V_s - R_s I_s) dt + \psi_r \quad (2.19a)$$

$$T_e = p(\psi_s I_s) \quad (2.19b)$$

With these states calculated, a simple hysteresis band is applied to each, torque and flux, to select one of the 8 possible voltage vectors. This selection is done based on a lookup table that depending

on the output of both hysteresis controllers, chooses the vector that pushes the torque and flux towards its references. This table can be generated using several strategies with different resultant dynamics [32, 33]. Note that the nature of only switching vectors when the hysteresis is surpassed results in a

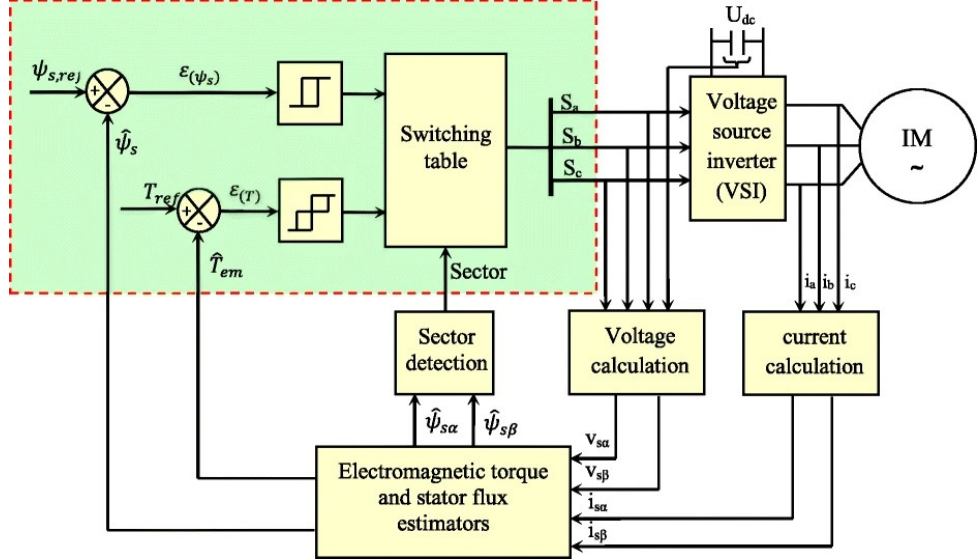


Figure 2.6: Direct Torque Control - from El Ouanjli et al. [34].

variable switching frequency as opposed to FOC that has a fixed switching frequency. Another feature of the DTC is that it does not need any modulators, as it directly chooses the voltage vector to be applied.

DTC is a very accessible method, with simpler implementation than FOC a faster dynamic response and low sensitivity to motor parameters, but it falls short in steady state operation with torque and current ripple often bigger than its rival FOC[35, 36].

2.4.3 Model Predictive Control

With the increase in computational power, the MPC has gained space between the machine controllers as it handles multivariable non-linear cases, is easy to design, has great dynamic response and integrates constraint managing[37]. The model predictive controller basic idea is to use a mathematical model of the controlled system to test several control actions and make a prediction about the system response. This prediction is then evaluated by a cost function that can include some soft constraints and the control action with the smaller cost is chosen as optimal. The process of finding an optimal control defines the controller topology. Vazquez et al. [8] classifies predictive controllers in power converters and drives into two topologies: continuous set, and finite set.

Continuous set is very similar to predictive controllers used on other control fields, it computes a continuous control signal and uses a modulator to generate these voltage vectors. This topology comes with the advantage of fixed switching frequency at the cost of harder formulation. The finite set topology explores the limited control options of power converters to simplify the optimization process. This topology tests a set of the possible control vectors (this set can contain all or part of the possible vectors), and evaluates each of the vectors based on the predictions. While simpler to formulate, this method

results in the chosen vector being applied to the full switching period, which results in a higher ripple when compared with a strategy that uses a modulator at the same control frequency. Another property of this strategy is the variable switching frequency, as the same vector can be chosen consecutively.

To reduce the problem of applying the vector for the full timestep, a subset of finite set topology was presented. It adds time as part of the equation by computing the optimal switching sequence instead of the optimal switching vector, similar to a modulator. This allows the controller to choose a set of vectors to be switched in a given sequence with a duration also chosen by the controller.

When applied to PMSM the predictive controllers are commonly designed with the dq0 model equation (2.14) [38], and may track the currents or the torque to a given reference. The current tracking computational cost tends to be lower as the current optimization can be done offline while tracking torque makes online parameter estimation easier. If the topology is chosen to be continuous, a solver needs to be designed, one of the approaches is to expand the model and cost function into Taylor series approximations, and then use the derivative of the cost function to create a control law [39].

Chapter 3

Implementation

Contents

3.1 Motor characterization	18
3.1.1 Phase resistance	19
3.1.2 Flux Linkage	19
3.1.3 Inductance method 1	20
3.1.4 Inductance method 2	23
3.2 Current References	26
3.2.1 Voltage Constraint	28
3.3 Load profile	30
3.4 Proposed Control Methods	31
3.4.1 Finite Set MPC	31
3.4.2 Finite Set with Null Vector MPC	31
3.4.3 Explicit Continuous Set MPC	33
3.4.4 Implicit Continuous Set MPC	33
3.5 Horizon Extension	34

3.1 Motor characterization

Although AMK has provided the motor datasheet with the key parameters on it, it is important to verify how well they track the real values, and how they change regarding the motor operation. The datasheet values are linear approximations of the magnetic circuit on the motor, and as such do not accurately represent the machine at high current operating points. To account for the saturation effect, a variable inductance approach will be used[40, 41], where the inductance of each axis will be a function of the current on the respective axis. As explained in chapter 2, this would result in an algebraic loop, so an approximation is used, where the inductances at k will be a function of the currents at $k - 1$.

To characterize the motor a few variables need to be defined, they are:

- Magnet flux linkage (ψ_{PM})
- Phase resistance (r)
- Direct and Quadrature inductances (L_d and L_q)

3.1.1 Phase resistance

The easiest one to measure is the phase resistance. Assuming the machine is well balanced, the phase resistance will be equal to $\frac{3}{2}$ of the terminal resistance. Although a multimeter can be used, it will give poor precision, as the resistance is very low, so it's better to use a milliohmmeter or even better a micro-ohmmeter. A good practice would be to evaluate the parameters at different temperatures, especially the resistance, but that would require some specific hardware that is currently not available for this work.

The used device was a *UNI-T UT620A Micro-ohmmeter*, that has a resolution of $10\mu\Omega$ with an accuracy of $\pm(0.25\% + 25\mu\Omega)$. The measurements were taken on the terminal wires at room temperature and with the kelvin probe, resulting in $142.89 \pm 0.06m\Omega$. This value is close to the datasheet one of $135m\Omega$, and the difference is probably due to the wire terminals. The resultant phase resistance (r) is $214.335 \pm 0.091m\Omega$.

3.1.2 Flux Linkage

The magnet flux linkage can be measured by externally rotating the rotor and measuring the generated back EMF. From equation (2.13), if the terminal wires are disconnected from everything, the current will be constantly zero, thus the measured voltage will be only a result of the flux linkage and the rotor velocity as shown in equation (3.1).

$$u_d = r_d j_d + \cancel{\frac{di_d}{dt}}^0 \left(L_d + j_d \cancel{\frac{\partial L_d}{di_d}}^0 \right) - \omega_e L_q j_q = 0 \quad (3.1a)$$

$$u_q = r_q j_q + \cancel{\frac{di_q}{dt}}^0 \left(L_q + j_q \cancel{\frac{\partial L_q}{di_q}}^0 \right) + \omega_e (L_d j_d + \psi_{PM}) = \omega_e \psi_{PM} \quad (3.1b)$$

Using an external device, the rotor was kept at a constant speed that was measured by the digital encoder in the AMK motor, while an oscilloscope (*Promax OD-571*) was connected to two terminal wires. The oscilloscope on the used settings has an accuracy of $\pm(3\% + 0.2508V)$. An example of the output is shown in figure 3.1(a).

In the example image, the oscilloscope measured a peak voltage of 10.2, while the rotor was spinning at 386rpm, which is equivalent to $202rad/s$ electrical velocity. This results in a flux linkage of $0.050Wb$. The same procedure was repeated at several speeds, and the results are shown in figure 3.1(b). In this graph, two other lines are shown, they represent the flux linkage estimated using the torque and speed constant provided in the datasheet. Notice that it aligns well with the voltage constant value, but it is

very different from the torque constant one. This is probably due to different standards being used, but as there isn't much information available on the datasheet, the measured value is assumed to be the correct one.

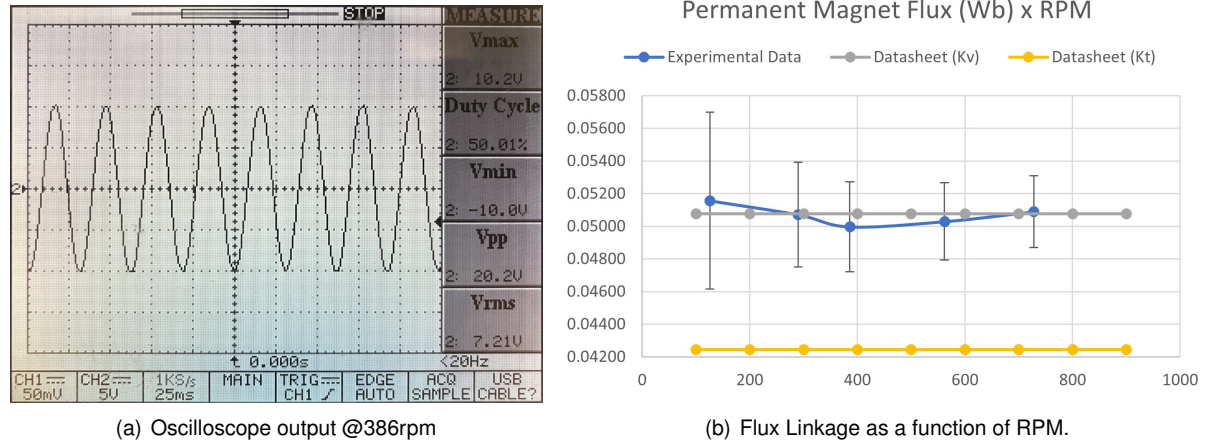


Figure 3.1: Flux Linkage characterization.

3.1.3 Inductance method 1

The inductance measurement is a little more complex, so to achieve better accuracy, two different methods will be proposed, one using the inverter, and the other only using a DC power supply.

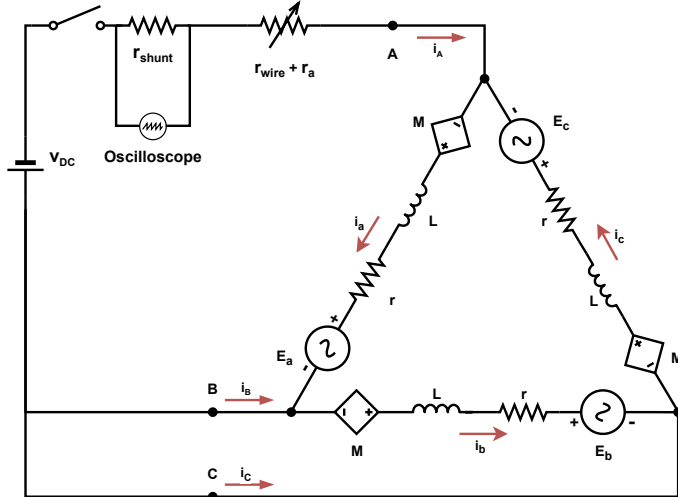


Figure 3.2: Inductance measurement setup schematic.

The simpler method, which does not use the inverter, works by measuring the current throughout a voltage step and measuring the time constant of the system. To measure the current, a shunt resistor is used coupled with the same oscilloscope from the previous section (*Promax OD-571*). To achieve a variable current, a variable resistor was used in series with the shunt, as shown in figure 3.2. The system resistance was measured with the micro ohmmeter from the previous section (*UNI-T UT620A Micro-ohmmeter*), including wire and switch resistance. The experiment setup is shown in figure 3.3.

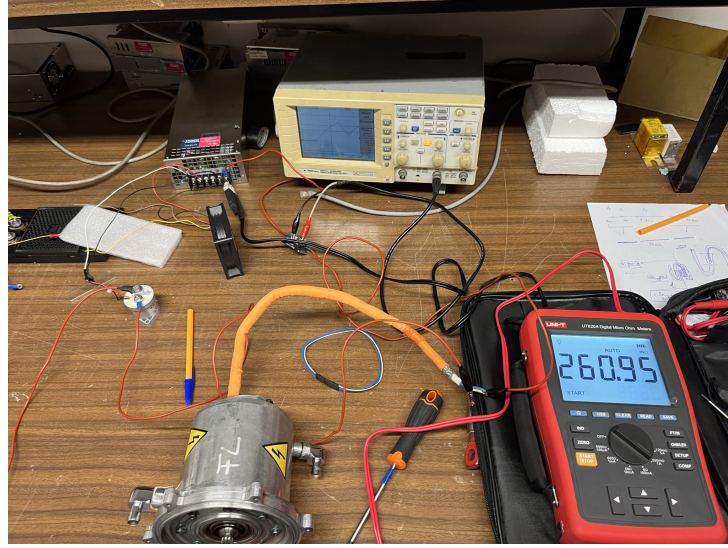


Figure 3.3: Inductance measurement setup.

Direct Axis

The direct axis measurement starts with the resistance measurement of the entire setup, motor, wires, switch, and shunt. Then, a quick voltage pulse is applied to align the rotor with the magnetic field, which in this setup is equivalent to the voltage vector V_6 . In the aligned condition, the current through phase b (i_b) is zero, and $i_a = -i_c$. After the rotor is aligned, a new pulse is done, now for the actual measurement as exemplified in figure 3.4. The time constant can be retrieved using the basic equation for an RL circuit applied to the shunt resistor (3.2a).

$$u(t) = i_A r_{shunt} (1 - e^{-\frac{t}{\tau}}) \quad (3.2a)$$

$$\tau = \frac{2L_d}{\frac{r}{2} + r_{wire} + r_a + r_{shunt}} \quad (3.2b)$$

In equation (3.2a) $u(t)$ represents the measured voltage on the shunt resistor, V_{DC} is the power supply voltage, τ is the system time constant, r_a is the variable resistance to adjust the current, r_{shunt} is the shunt resistance, and r_{wire} is the sum of the wire resistances with the switch resistance. To simplify the measurements, instead of calculating the first term $i_A r_{shunt}$, it was replaced by the voltage that which the oscilloscope settled.

With the curve plotted on the oscilloscope, the time constant was measured by evaluating how long it took for the voltage to reach $0.632i_A r_{shunt}$. Then, with the time constant and the system resistance, the inductance was calculated. Note that this inductance was measured for a phase current of half the line current, resulting in a direct axis current of $i_d = \frac{i_A}{\sqrt{3}}$.

The inductance variation with current is not symmetrical in the current axis, as the permanent magnet offsets the magnetic curve, causing saturation with very small positive currents in the direct axis. Although simple, this method has the drawback of not measuring the variation of inductance in the field weakening operating range, only on the field intensifying range that is not often used. To measure in the field weakening range it is necessary to lock the rotor after the initial pulse, and then invert the power

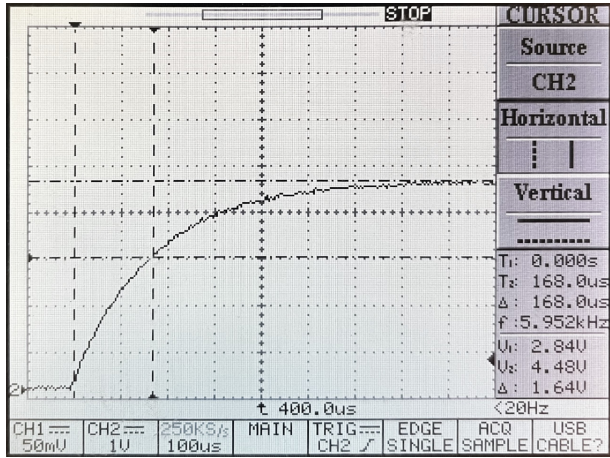


Figure 3.4: Inductance measurement oscilloscope output.

supply polarity.

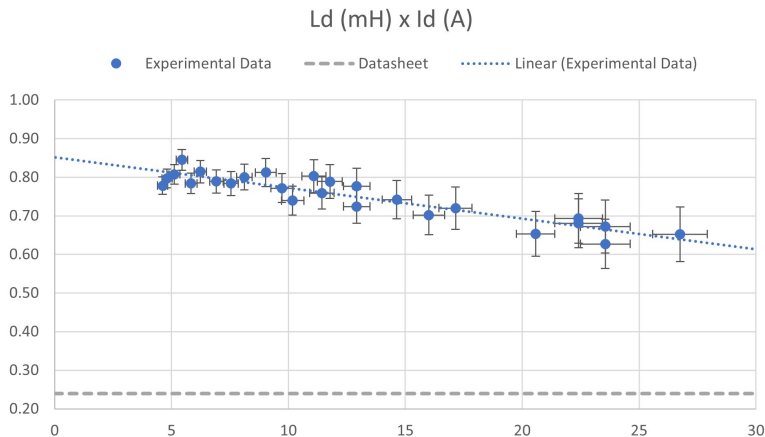


Figure 3.5: L_d in function of i_d .

The test results are shown in figure 3.5, and as with the flux linkage, there is a great difference between the measured data and the value from the datasheet. The saturation effects are clear and start with very little current, as predicted.

Quadrature Axis

The quadrature axis measurement is very similar to the direct axis, showing only two differences. The first one is that the alignment pulse is not applied with the default connection, as with the direct axis, but only connects on two terminals, as shown by figure 3.6. This will align the rotor with the phase b axis. The second difference is that after the alignment, an external tool is necessary to lock the rotor in place. This allows quadrature current to be applied without the resultant torque changing the position of the rotor.

The results of the quadrature inductance are shown in figure 3.7. It is important to note that as there isn't a reminiscent magnetic flux in the quadrature axis, the variation of the inductance with current is symmetrical in the current axis, and only shows signs of saturation at high currents.

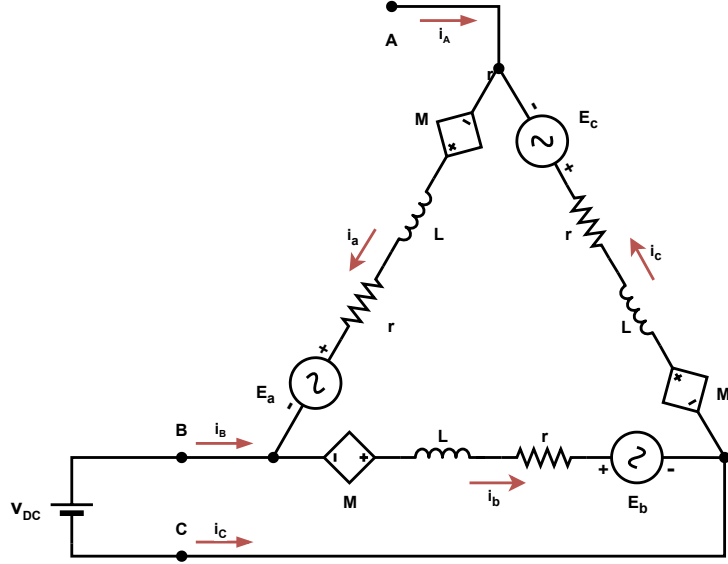


Figure 3.6: Quadrature Inductance measurement alignment pulse setup.

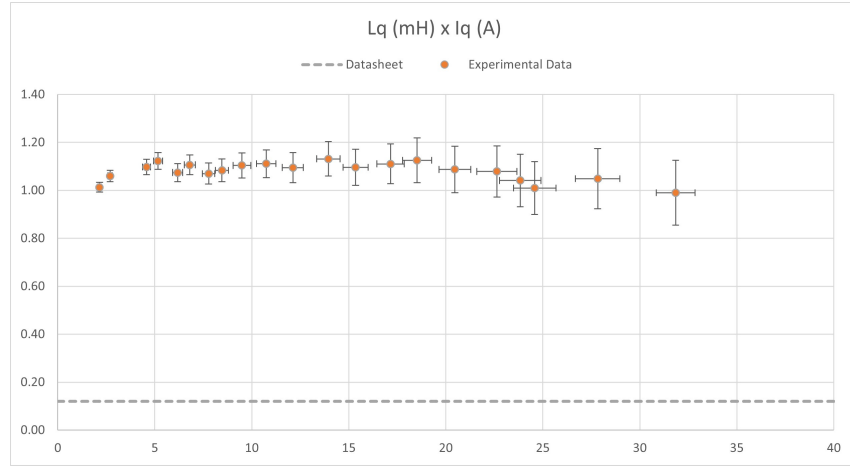


Figure 3.7: L_q in function of i_q .

3.1.4 Inductance method 2

The second method for inductance characterization is according to Stumberger et al. [41]. It uses a VSI coupled with a control algorithm to keep the current in one of the axis constant, and then do a step in the voltage on the other axis. This test also needs to be done in a locked rotor position, but it has the advantage of characterizing the cross-magnetization effect.

$$u_d = ri_d(t) + \frac{d\psi_d(t)}{dt} - \psi_q \omega_e \vec{e}^0$$

$$u_q = ri_q(t) + \frac{d\psi_q(t)}{dt} + (\psi_d + \psi_{PM}) \omega_e \vec{e}^0$$

$$\frac{d\psi_d(t)}{dt} = u_d - ri_d(t) \quad (3.4a)$$

$$\frac{d\psi_q(t)}{dt} = u_q - ri_q(t) \quad (3.4b)$$

This method defines the flux linkage based on the integration of equation (3.4), and to measure the flux linkage variation in the quadrature axis, it performs a series of stepwise voltage changes in u_q while maintaining the current i_d constant (figure 3.8). The integration of those curves will result in the quadrature flux linkage variation with i_q . These steps are repeated for several values of i_d , and for each of them, a flux linkage curve is created as shown in figure 3.9.

Instead of using the measured value for the phase resistance, its value is estimated by assuming the current is at a steady state at the end of the voltage pulse so that the flux linkage is stable and $u_x = ri_x$, this is done to reduce integration errors on the flux linkage and also to account for wires, connections, and mosfet resistances.

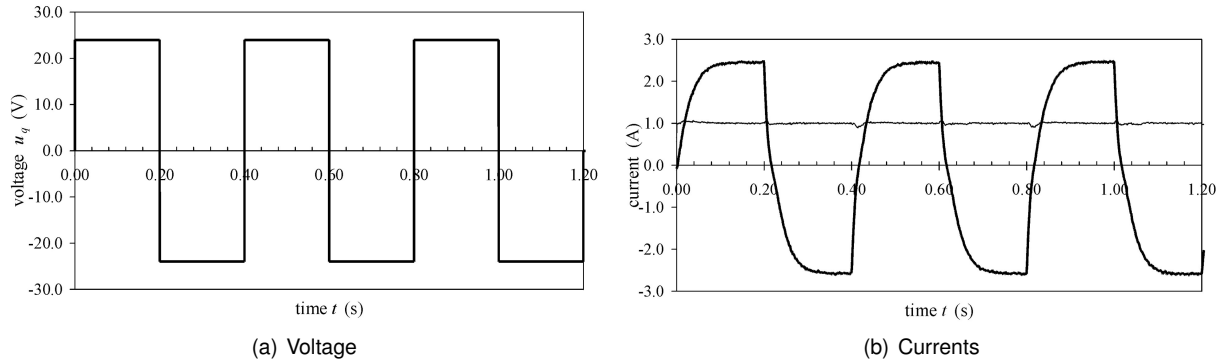


Figure 3.8: Identification voltage pulses - from Stumberger et al. [41].

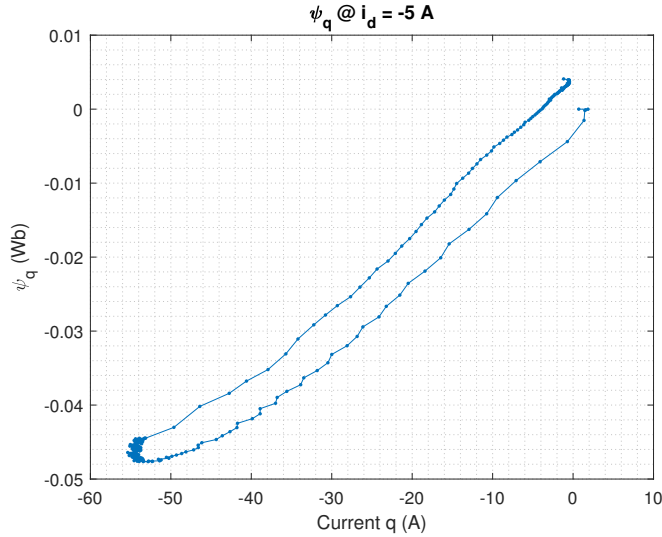


Figure 3.9: Quadrature Flux linkage @ $i_d = -5A$.

The same procedure is used for measuring ψ_d , but this time the quadrature current is fixed and the direct voltage is changed in stepwise form. Although the original method is proposed to characterize crossmagnetization effects, the results shown in figure 3.10 presents little variation with currents on the perpendicular axis, thus to simplify the study they are approximated as independant.

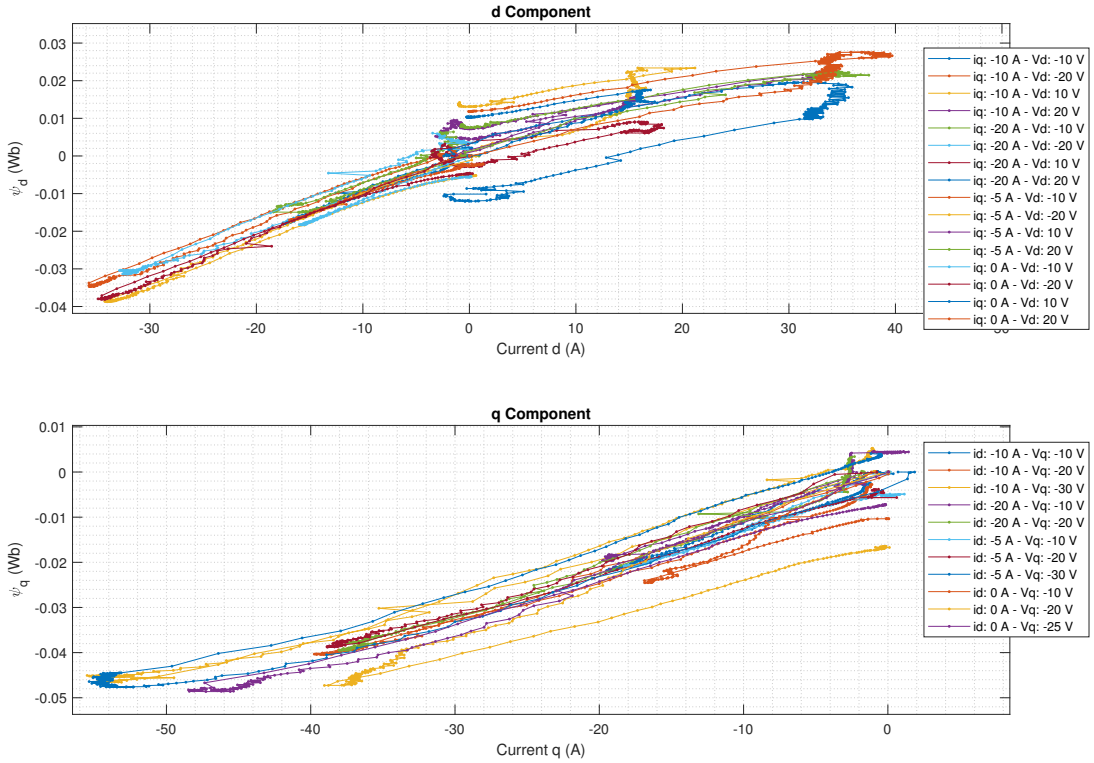


Figure 3.10: Flux linkage with different currents on perpendicular axis.

After the characterization of the fluxes, an exponential fit is made to allow for analytical differentiation, and the derivative is taken to find the inductances, as shown in equation (3.5).

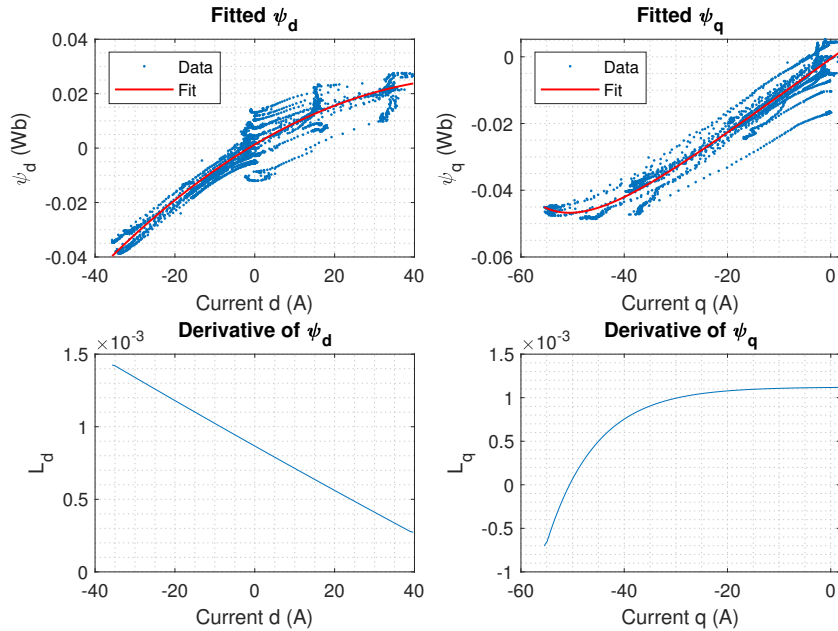


Figure 3.11: Flux Linkage exponential fit.

$$L_d = \frac{\partial \psi_d}{\partial i_d} \approx \frac{\Delta \psi_d}{\Delta i_d} \quad (3.5a) \qquad L_q = \frac{\partial \psi_q}{\partial i_q} \approx \frac{\Delta \psi_q}{\Delta i_q} \quad (3.5b)$$

The resultant inductances are shown in figure 3.11. Ideally, this test should be performed with a voltage pulse big enough to cover the full current range of the machine, but the available hardware was not capable of reaching such currents, thus the limited range. Note that the lack of current range resulted in a poor fit, mostly after the 40A, on the quadrature axis, with the inductance dropping to a negative value. Despite the limitations, the inductance values using this method closely match with the ones found using method 1 from section 3.1.3. This not only increases the confidence in the results but also enables the formulation of a calibration routine on the inverter software that, given some adaptations, can calculate all the motor parameters within a few minutes.

3.2 Current References

Although it is possible to use the MPC to optimize the current references, doing it offline not only allows for faster computational times but also results in more precise references. The downside of this approach is that it negates the possibility of acting upon online parameter estimation, but in a development prototype as a formula student vehicle, that is not much of a problem if a proper calibration procedure is implemented.

As efficiency is one of the objectives, a good approach is to maximize the torque generated by a given current $i = \sqrt{i_d^2 + i_q^2}$. This strategy is called Maximum Torque per Ampere (MTPA), and when there aren't constraints it becomes a simple problem defined in equation (3.6).

$$\begin{aligned} \max_{i_d, i_q} \quad & p i_q ((L_d - L_q) i_d + \psi_{PM}) \\ \text{s.t.} \quad & i = \sqrt{i_q^2 + i_d^2} \end{aligned} \quad (3.6)$$

To optimize 3.6, one can write the problem using Lagrange multipliers (λ):

$$\mathcal{L} = p i_q ((L_d - L_q) i_d + \psi_{PM}) - \lambda (\sqrt{i_q^2 + i_d^2} - i) \quad (3.7)$$

Thus the partial derivatives become:

$$\frac{\partial \mathcal{L}}{\partial i_d} = p i_q (L_d - L_q) - \frac{\lambda i_d}{\sqrt{i_d^2 + i_q^2}} \quad (3.8a)$$

$$\frac{\partial \mathcal{L}}{\partial i_q} = p ((L_d - L_q) i_d + \psi_{PM}) - \frac{\lambda i_q}{\sqrt{i_d^2 + i_q^2}} \quad (3.8b)$$

$$\frac{\partial \mathcal{L}}{\partial \lambda} = \sqrt{i_q^2 + i_d^2} - i \quad (3.8c)$$

Now, equating the partial derivatives to zero, and replacing equation (3.8a) in equation (3.8b) and equation (3.8c):

$$i = \sqrt{i_q^2 + i_d^2} \quad (3.9a)$$

$$\frac{\lambda i_d}{i} = p i_q (L_d - L_q) \quad (3.9b)$$

$$\frac{\lambda i_q}{i} = p((L_d - L_q)i_d + \psi_{PM}) \quad (3.9c)$$

Isolating λ in equation (3.9c) and replacing it on equation (3.9b):

$$\frac{p((L_d - L_q)i_d + \psi_{PM})i_d}{i_q} = p i_q (L_d - L_q) \quad (3.10)$$

Rearranging to a quadratic form:

$$i_d + i_d^2 \frac{L_d - L_q}{\psi_{PM}} = i_q^2 \frac{L_d - L_q}{\psi_{PM}} \quad (3.11)$$

Solving for i_d

$$i_d = \pm \frac{\sqrt{4 \left(\frac{L_d - L_q}{\psi_{PM}} \right)^2 i_q^2 + 1} - 1}{2 \frac{L_d - L_q}{\psi_{PM}}} \quad (3.12)$$

But comparing with the torque equation is clear that the negative option would not maximize the torque, thus:

$$i_d = \frac{\sqrt{4 \left(\frac{L_d - L_q}{\psi_{PM}} \right)^2 i_q^2 + 1} - 1}{2 \frac{L_d - L_q}{\psi_{PM}}} \quad (3.13)$$

This equation is valid for a constant inductance and with no constraints. If the inductance curve is assumed to be monotonically decreasing, using an iterative approach the algebraic loop of the inductances can be solved, and the reference calculated, resulting in figure 3.12.

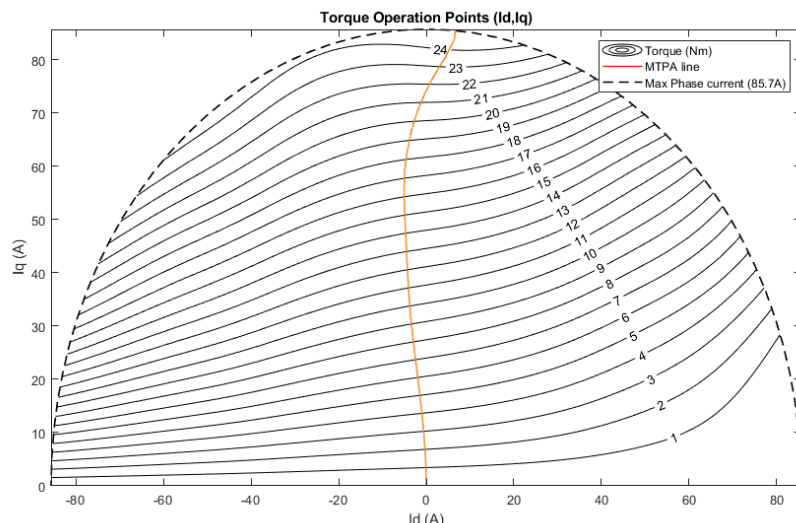


Figure 3.12: Maximum Torque per Ampere curve without constraints.

3.2.1 Voltage Constraint

While simple, the presented approach does not account for voltage limitations, where with the increase in velocity, the back emf becomes large enough to limit the current operation points. To account for that the voltage constraint must be defined.

If the current is assumed to be constant, equation (2.14) can be rearranged to calculate the maximum current for a given voltage and velocity:

$$u_d = ri_d - \omega_e L_q i_q \quad (3.14a)$$

$$u_q = ri_q + \omega_e (L_d i_d + \psi_{PM}) \quad (3.14b)$$

$$\sqrt{u_d^2 + u_q^2} \leq V_{dc} \quad (3.15)$$

Subjecting equation (3.14) to equation (3.15) an ellipse equation is found:

$$(ri_d - \omega_e \psi_q)^2 + (ri_q + \omega_e \psi_d^*)^2 \leq V_{dc}^2$$

Where $\psi_d^* = L_d i_d + \psi_{PM}$ and $\psi_q = L_q i_q$. Note that this ellipse dynamically changes throughout the use of the motor based on the speed and the DC link voltage.

Using the ellipse as a constraint, equation (3.6) can be rewritten as in equation (3.16), where the speed and DC link voltage are known.

$$\begin{aligned} \min_{i_d, i_q} \quad & \sqrt{i_q^2 + i_d^2} \\ \text{s.t.} \quad & T_{ref} = p i_q ((L_d - L_q) i_d + \psi_{PM}) \\ & (ri_d - \omega_e \psi_q)^2 + (ri_q + \omega_e \psi_d^*)^2 \leq V_{dc}^2 \end{aligned} \quad (3.16)$$

This optimization problem was formulated on *MATLAB* for several speeds and voltages. Some of the main cases are shown in figure 3.13. On this graph, the iso-torque lines show the current combinations that yield the same torque, independent of the velocity or the voltage. The voltage ellipses are defined from the rotor velocity and the current DC link voltage, and they assume that the current is constant. The area contained by the ellipse is the feasible region at that speed and supply voltage. Steady-state operation at any point outside the ellipse would require a speed reduction or a voltage increase.

Note that while the torque map is symmetrical relating to the i_d axis, the voltage ellipse is not, it has been rotated slightly in an anti-clockwise direction. This rotation is due to the resistance of the phases that when accelerating, reduce the total available voltage to fight the back EMF. If the phase resistance is low the ellipse becomes aligned with the i_d axis. Another important remark is the center of the voltage ellipse, as the AMK motor has permanent magnets with strong flux linkage the ellipse center is shifted farther away from the origin, but in a reluctance machine, the center would be at the origin, the same as the torque. Special cases appear when the ellipse center is inside the feasible current region, as the voltage-limited speed goes to infinity. An important location in this graph is the motor characteristic

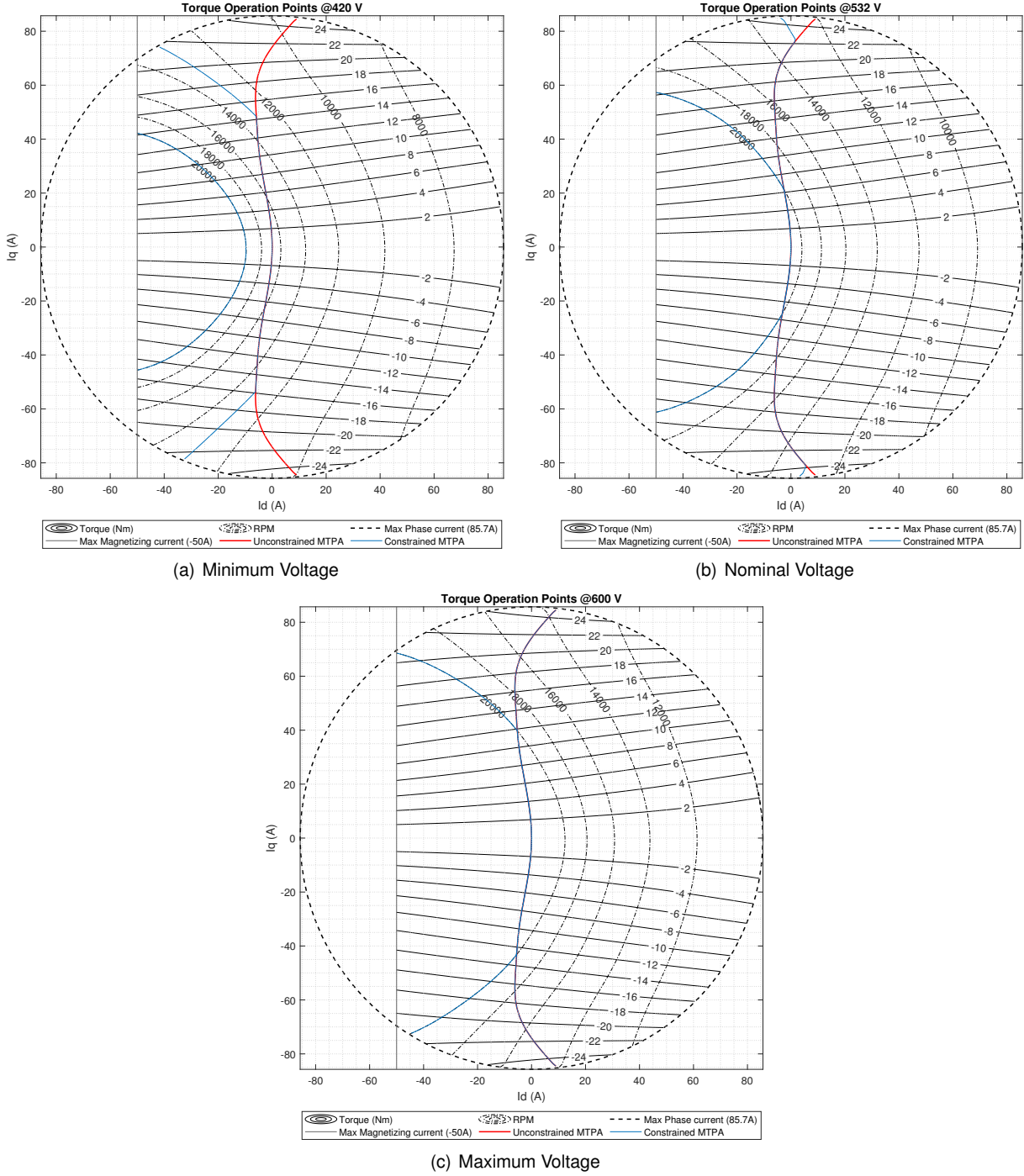


Figure 3.13: Constrained Maximum Torque per Ampere curve at minimum, nominal, and maximum voltages.

point, which can be easily located as being the place where the maximum phase current circumference yields the higher torque. The speed at this point is the motor's characteristic speed, and if the graph is created for the motor's nominal voltage, that becomes also the nominal speed of the motor. This point is important as any further increase in speed will result in a reduction in the maximum motor torque.

Figure 3.13 clearly shows that the optimal current reference is the MTPA while the velocity and voltages allow it, and after that, the voltage ellipse becomes the best alternative. It is important to understand that the voltage constraint is dependent on the combination of DC Link voltage and rotor

speed, when the voltage increases the ellipse for a given speed expands, allowing further operation on the unconstrained MTPA line. This not only increases efficiency (as it produces the same torque with less current) but also improves performance, pushing the motor characteristic point further on the torque vs rpm diagram.

Some processing is still needed to account for points outside of the feasible region, but the presented graphs can be used as a motor map, where given the current DC Link voltage, motor speed, and desired torque, it returns the reference currents to optimally reach the torque reference. This can also be expanded to include temperature effects.

3.3 Load profile

To derive a representative load profile for the motor a car model is necessary. In this case, a simple one-dimensional model is used in equation (3.17).

$$(m_{car} + m_{wheel\,equivalent}) a_x = F_{motor}\eta_{transm} - F_{rolling\,resistance} - F_{drag} \quad (3.17)$$

Where the rolling resistance is a constant force that depends on the rolling resistance coefficient and the weight of the car (equation (3.19)), the losses are neglected, and the aerodynamic drag is calculated as in equation (3.18).

$$F_{drag} = 0.5\rho C_d A_r v^2 \quad (3.18)$$

$$F_{rolling\,resistance} = C_r m_{car} g \quad (3.19)$$

To calculate the inertia seen by the motor, an equivalent rotational inertia must be computed. To do that, the energy stored in the rotating parts and on the car is equated with the equivalent inertia as shown in equation (3.21).

$$\begin{aligned} \frac{1}{2} J_{eq} \omega^2 &= \frac{1}{2} m_{car} v^2 + \frac{1}{2} J_{wheels} \omega^2 \\ \frac{1}{2} J_{eq} \omega^2 &= \frac{1}{2} m_{car} (\omega_{wheels} r_{tire})^2 + \frac{1}{2} J_{wheels} \omega_{wheels}^2 \\ \frac{1}{2} J_{eq} \omega^2 &= \frac{1}{2} m_{car} \left(\frac{\omega}{Gr} r_{tire} \right)^2 + \frac{1}{2} J_{wheels} \left(\frac{\omega}{Gr} \right)^2 \\ \frac{1}{2} J_{eq} \omega^2 &= \frac{1}{2} \left(\frac{m_{car} r_{tire}^2}{Gr^2} + \frac{J_{wheels}}{Gr^2} \right) \omega^2 \end{aligned} \quad (3.20)$$

$$J_{eq} = \frac{m_{car} r_{tire}^2 + J_{wheels}}{Gr^2} \quad (3.21)$$

From experimental tests with previous prototypes, a rule of thumb is that when accelerating only one-third of the power can be applied at the front axle, while the rear axle receives two-thirds. Ideally, a weight transfer function would be used, but to simplify the equations the constant distribution will be used. Thus the equivalent rotational inertia at each motor is on equation (3.22).

$$J_{f_{eq}} = \frac{m_{car} r_{tire}^2 + 6 J_{wheel}}{6 Gr^2} \quad (3.22a) \qquad J_{r_{eq}} = \frac{m_{car} r_{tire}^2 + 3 J_{wheel}}{3 Gr^2} \quad (3.22b)$$

Combining the equations, a torque profile is defined in equation (3.23).

$$J_{f_{eq}} \dot{\omega} = T_{motor} \eta_{transm} - \frac{(F_{rolling\ resistance} + F_{drag}) r_{tire}}{6 Gr} \quad (3.23a)$$

$$J_{r_{eq}} \dot{\omega} = T_{motor} \eta_{transm} - \frac{(F_{rolling\ resistance} + F_{drag}) r_{tire}}{3 Gr} \quad (3.23b)$$

3.4 Proposed Control Methods

This work proposes 4 different predictive control strategies that were compared with the manufacturer's FOC and one of them was selected for implementation. The approaches are:

- Finite Set MPC
- Finite Set with null vector MPC
- Explicit Continuous Set MPC
- Implicit Continuous Set MPC

All of those utilize the latest measurement of line currents to estimate each of the phase currents and, using the rotor position encoder data a Blondel-Park transformation can be applied to get the direct and quadrature currents. Also from the rotor position encoder, the rotor velocity is measured. Additionally, the current DC-link voltage is also measured to account for battery voltage fluctuation. This processed data is refreshed at each time step and utilized on the selected control strategy. Although it is possible to use multiple horizon steps, to keep the computational cost low, and maintain high switching frequencies, all the proposed methods use a horizon of only 1 time step. This is later verified as not having an expressive take on performance as the system is fast enough so that the dynamics are well represented with only one timestep.

3.4.1 Finite Set MPC

In a FS-MPC each of the vectors defined on table 2.2 are applied to equation (2.17) using the current measured data, resulting in different predictions for the next time step values. A cost function that compares the torque and currents (to account for MTPA) with the references, is then evaluated for each of those predictions. The vector with the lowest cost is then applied at the next time step, as shown in figure 3.14.

3.4.2 Finite Set with Null Vector MPC

Although effective, the simple Finite Set MPC can incur heavy torque ripple, due to its limited options on which vector can be applied. That behavior can be exacerbated by low power operation points, where the active vectors result in a bigger percentual change in currents. This problem can be mitigated by

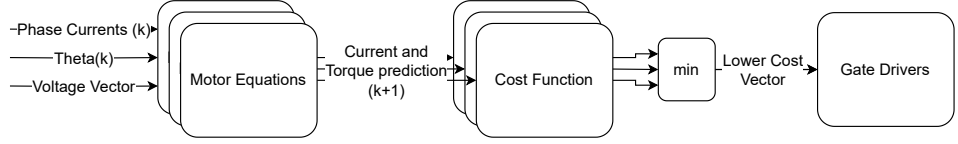


Figure 3.14: FSMPC Diagram.

introducing the possibility of sharing the sample time between the chosen active vector and a null vector. Such an approach allows the control to apply vectors that point in the direction of the native ones but have smaller amplitude.

This addition of a null vector comes with the problem of now having virtually infinite vector options (depending on the PWM resolution), but that can be solved with a few tricks. This new system starts as the previous one, where each of the 7 possible vectors is applied to the motor model, but before passing those results for the cost function a simple check of torque is made. If the values of torque at k and $k + 1$ are at different sides of the torque reference the algorithm realizes that the ideal vector has a smaller amplitude, thus trying to compute a ratio of active vector time and null vector time. To calculate such a ratio an approximation was made, given the short sample time, the complete system is assumed to behave linearly during that period. If the system behaves linearly, the currents and torque for a combination of null and active vectors will also be a linear combination of the individual values for each vector multiplied by its application time.

$$i_x = i_a d_a + i_n d_n \quad (3.24)$$

$$T_x = T_a d_a + T_n d_n = T_a d_a + T_n - T_n d_a \quad (3.25)$$

With that property, knowing that $d_a + d_n = 1$ the duty cycle for the active vector becomes:

$$d_a = \frac{T_{ref} - T_n}{T_a - T_n} \quad (3.26)$$

With the duty cycle calculated, the predictions are updated and passed to the cost function, which chooses the best combination of active and null vectors.

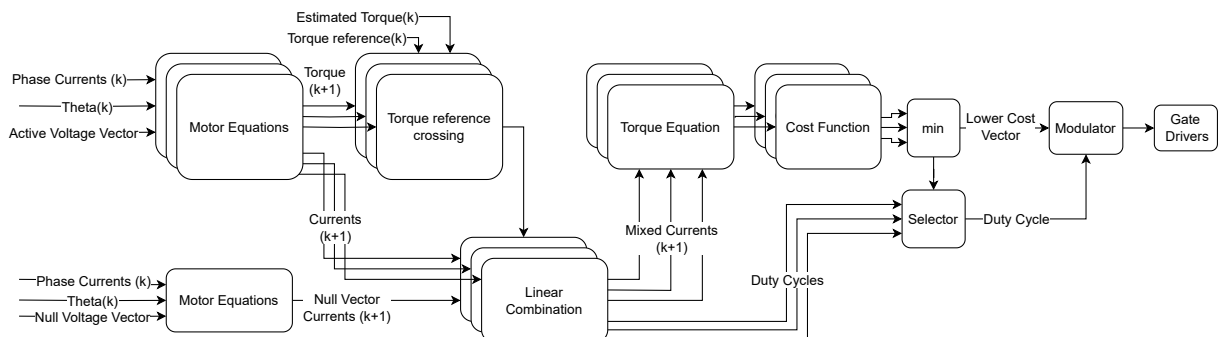


Figure 3.15: Finite Set with Null Vector MPC Diagram.

3.4.3 Explicit Continuous Set MPC

One of the advantages of the approximations made in the discretization process is that even though the matrices change in time, for a given moment the system is linear, and as such an inverse dynamic can be derived. So, if in equation (2.17) the currents on the next step are replaced by a reference for the current vector, the necessary applied voltage can be calculated:

$$\begin{aligned} \begin{bmatrix} u_{d(k+1)} \\ u_{q(k+1)} \end{bmatrix} &= \begin{bmatrix} \frac{h}{hr+L_{d(i_d(k))}} & 0 \\ 0 & \frac{h}{hr+L_{q(i_q(k))}} \end{bmatrix}^{-1} \\ \left(\begin{bmatrix} 1 & -h \frac{\omega_e(k) L_{q(i_q(k))}}{hr+L_{d(i_d(k))}} \\ h \frac{\omega_e(k) L_{d(i_d(k))}}{hr+L_{q(i_q(k))}} & 1 \end{bmatrix} \begin{bmatrix} i_{dref} \\ i_{qref} \end{bmatrix} - \begin{bmatrix} \frac{L_{d(i_d(k))}}{hr+L_{d(i_d(k))}} & 0 \\ 0 & \frac{L_{q(i_q(k))}}{hr+L_{q(i_q(k))}} \end{bmatrix} \begin{bmatrix} i_{d(k)} \\ i_{q(k)} \end{bmatrix} - \begin{bmatrix} 0 \\ -h \frac{\omega_e(k) \psi_{PM}}{hr+L_{q(i_q(k))}} \end{bmatrix} \right) \end{aligned} \quad (3.27)$$

This approach is commonly used in linear unconstrained MPCs to improve computation times, where a control law is precomputed and stored in memory. But in the presented case there is an important constraint that is not accounted for in the previous equation. When very short time steps are used, and there is a big reference change, the necessary voltage to achieve the target on just one time step can be very high. This would lead to problems, like distortions due to overmodulation or not being able to reach the desired voltages. The solution to this problem is to saturate the voltage vector. Some authors have suggested saturating based on the closest possible vector [42], in this work, the saturation only limits the vector amplitude to match the DC-link voltage, maintaining the desired vector angle.

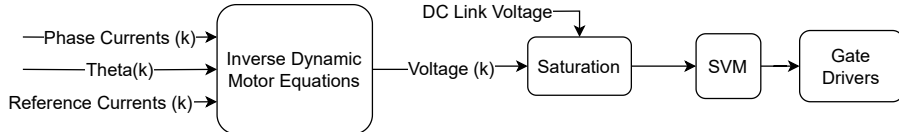


Figure 3.16: Explicit Continuous Set MPC Diagram.

This method greatly reduces the time taken to compute the control action, as instead of trying 7 different possible inputs (or more) it just calculates one time the necessary voltage and clamps it to the attainable values. As this control uses a continuous set, those values are then forwarded to a SVM system to modulate the Pulse Width Modulator (PWM) signals.

3.4.4 Implicit Continuous Set MPC

For the implicit approach, instead of resolving the equation to directly calculate the optimal control action, an iterative approach is used. As the system is not solved offline it is necessary to utilize an online solver that numerically optimizes the control action. This MPC technique has the advantage of easy constraints implementation, while still being a continuous set controller. This advantage comes at the cost of largely increased computational time, as it needs to evaluate the model equation several times to find the optimal voltage vector that fulfills the constraints. This additional complexity can often be prohibitive for power systems where a fast-acting control is needed.

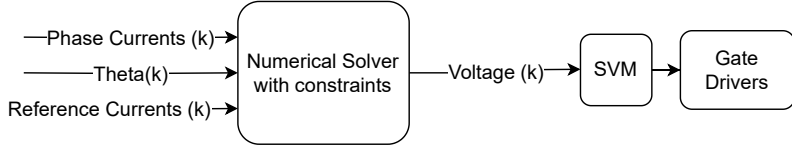


Figure 3.17: Implicit Continuous Set MPC Diagram.

3.5 Horizon Extension

A previously overlooked problem is the compensation of the computational time, as the acquisition and control calculations cannot be done instantly their delay needs to be compensated. The strategy adopted here is to use the motor model equations equation (2.17) coupled with the previously calculated control action to predict the system state in the next time step. Usually, this is done in a fixed timestep manner, where the predictive controllers instead of picking the control action for k in the timestep k , pick the control action for $k+1$ in the timestep k , as shown in equation (3.28) where x represent the currents, u is the voltage vector, A , B , C , and D are the matrixes and vectors of the model in equation (2.17) and are all dependent on the prediction duration $h = \frac{1}{f_{sw}}$.

$$x_{k+1} = A^{-1} (Bx_k + Cu_k + D) \quad (3.28)$$

For this equation to work the system timeline needs to be as in figure 3.18, starting with taking the current and voltage measurements, followed by applying the voltage vectors calculated in $k-1$, then extending the horizon by one timestep, and calculating the voltage vector for the next timestep[37].

This can be improved by only extending the horizon by the necessary time to compute the control action, this way the prediction error derived from model mismatch is reduced because the amount of time to predict is smaller. To do that the prediction duration is simply reduced to $h = t_{control}$, while the system timeline is shifted as in figure 3.19. The final control cycle starts with sensor acquisition,

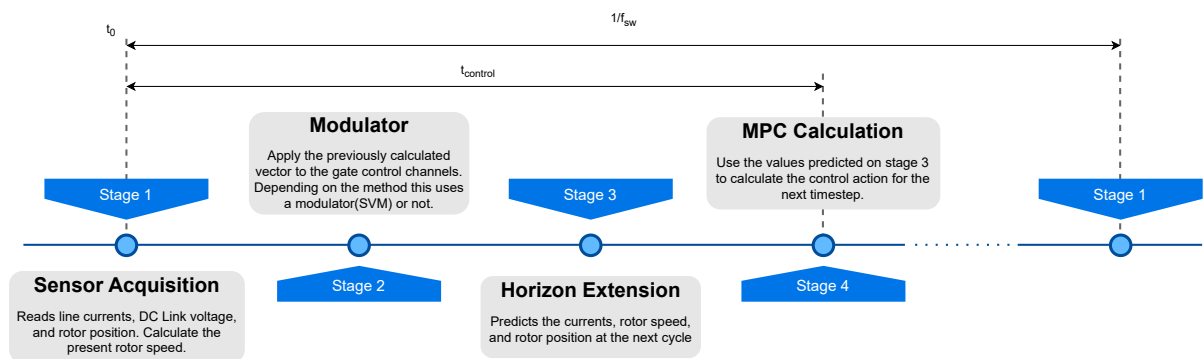


Figure 3.18: Horizon extension by one timestep.

followed by horizon extension, and lastly the future control action computation. Note that this delay is not a problem with simulation in *Simulink*, as it can instantly do the calculations, but it is good practice to

simulate it with the proper delays to increase the similarity between simulation and experimental results.

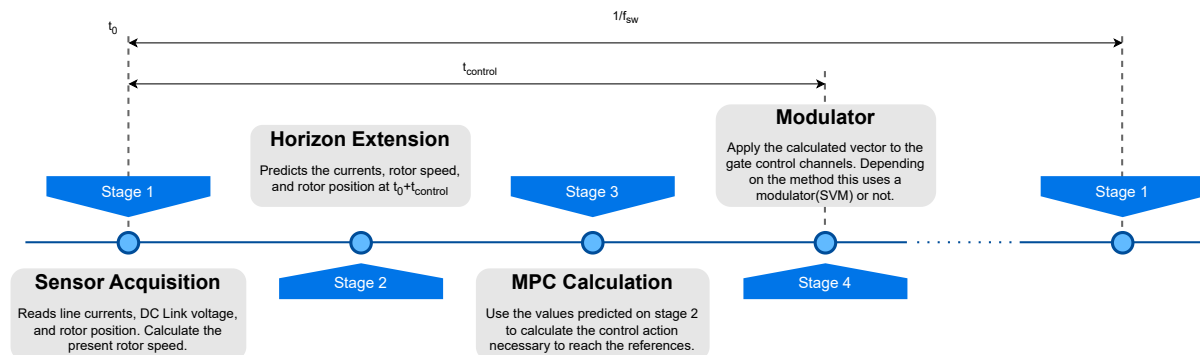


Figure 3.19: Horizon Extension by control time.

Chapter 4

Implementation

Contents

4.1 Simulation	36
4.2 Simulation vs Bench Tests	40

4.1 Simulation

To accelerate the development time, a virtual model was developed in *Simulink*, allowing for faster prototyping and direct comparison of the methods in a controlled environment. An adaptation of the *Simscape Specialized Power Systems* block *Permanent Magnet Synchronous Machine* was made to convert it to a delta-wound machine and to accept variable inductances as in equation (2.18). This model was combined with six MOSFETs blocks in three half-bridge configurations to simulate the VSI. To supply the MOSFETs, a representation of the battery was made, where an ideal voltage source is connected through a series resistor to the DC link, where a capacitor stabilizes the voltage. In figure 4.1 the resultant system is presented, where AU , AL , BU , BL , CU , CL , are the gate control signals that come from the control strategy.

The MOSFETs used in the simulation are derived from Wolfspeed C2M0040120D, as the one used on Costa[5]. The motor model is the one derived on section 2.3, with the parameters from section 3.1. The DC link capacitor is set to $40\mu F$, while the battery series resistance is 0.03Ω . The ground connections are $420k\Omega$ each, to simulate the isolation between high voltage and low voltage in the car, while the inertia and torque source blocks inside the motor area are to simulate the testbench environment, with the standard value of $0.0848kgm^2$ to the inertia, and the torque source being controlled to maintain a constant speed.

With the model implemented on *Simulink*, a baseline was made using the manufacturer control scheme, FOC with the standard 8kHz switching frequency, and compared with the proposed methods at 50kHz. The difference in frequency is to account for the complete system, where the use of widebandgap semiconductors allowed for a faster switching frequency. The baseline profile is a positive

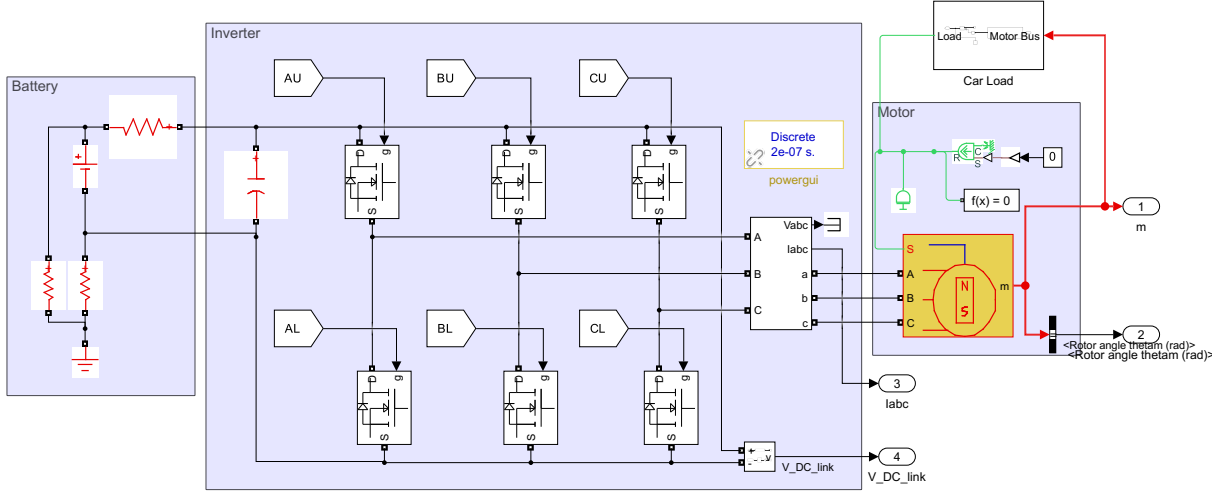


Figure 4.1: Simulink Models, Motor and Inverter.

torque step with the machine fixed at the nominal speed of 12kRPM. The rising time of each method is shown in figure 4.2.

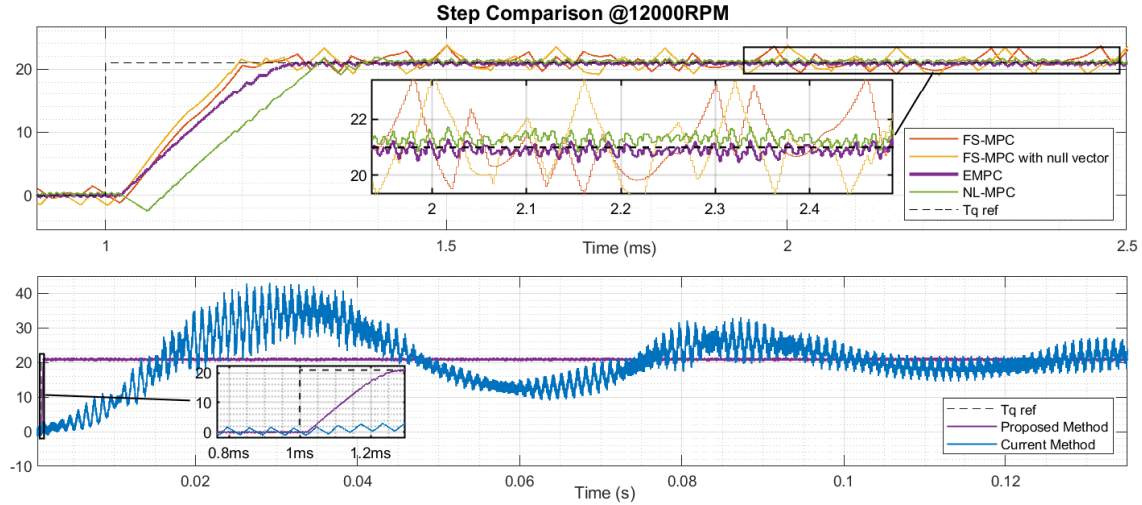


Figure 4.2: Torque step response.

Note that the predictive controllers all perform similarly, having a great dynamic response, with an average rising time (0 to 100%) of $200\mu s$, while the FOC method performed much slower, at approximately $180ms$. While the rising time in the FOC can be improved by better tuning the PID (these results are with the values recommended by the manufacturer), it would result in more pronounced overshoots and settling time, and would not reach the performance of a predictive controller, where the torque rising is only limited by the machine inductances, which shows the great dynamic performance of predictive controllers. It is important to also notice a small delay in the implicit MPC response, this delay is due to the solver failing to converge. Although this may not always occur at the step, it was intentionally left on this graph to remind us of the possibility of this event.

Divergence among the proposed methods becomes apparent during the analysis of steady-state

conditions. The basic FS-MPC stands out with the highest torque and current ripple, significantly worse than the baseline, rendering it impractical. This ripple is due to the absence of a modulator, thus the chosen vector will stay applied for the full sampling time. Although an increase in switching frequency would improve the absolute performance of this method, in comparison it would never be as smooth as a modulated control, as it uses discrete vector options, while a simple SVM would switch multiple times in a single period. The increased switching reduces the ripple at the cost of lowered efficiency due to switching losses.

The addition of the null vector on the second method reduces the ripple at low angular speeds but still fails to do so when the machine accelerates, with curves very similar to the FS-MPC. The use of complete modulators can reduce this torque ripple problem, as the SVM allows for a third vector to be applied during the same time step, allowing the control to accurately point the voltage vector to the desired angle and amplitude, where the null vector only lets the controller change the amplitude of the existent active vectors.

Table 4.1: Control Method Current THD comparison

		1000 RPM	7333 RPM	13666 RPM	20000 RPM
FOC @8kHz	1Nm	57.62%	43.44%	207.54%	29.62%
	11Nm	3.22%	10.62%	12.14%	58.53%
	20Nm	5.15%	6.50%	10.18%	37.08%
FOC @50kHz	1Nm	56.95%	11.08%	14.12%	4.71%
	11Nm	2.18%	2.19%	1.93%	4.85%
	20Nm	1.41%	1.41%	2.28%	3.86%
FS-MPC @50kHz	1Nm	696.41%	566.94%	247.13%	72.31%
	11Nm	39.42%	30.17%	28.04%	11.82%
	20Nm	22.10%	16.88%	8.52%	11.82%
FS-MPC	1Nm	30.67%	120.31%	159.20%	221.12%
Null Vector @50kHz	11Nm	1.59%	10.65%	12.40%	11.51%
	20Nm	1.76%	6.43%	7.10%	8.54%
EMPC @50kHz	1Nm	7.20%	11.91%	16.82%	21.95%
	11Nm	0.76%	1.47%	1.92%	2.16%
	20Nm	0.81%	0.98%	1.19%	1.12%
NL-MPC @50kHz	1Nm	6.59%	9.98%	12.60%	14.50%
	11Nm	0.81%	1.48%	1.89%	2.17%
	20Nm	0.81%	0.96%	1.18%	1.12%

When looking at the currents in table 4.1, the THD of the continuous MPC alternatives are expressively smaller than the baseline and the finite set MPCs, backing up the ripple analysis previously made. As expected the addition of a null vector reduced expressively the THD in operation points of low modulation index, but made no difference when the modulation index increased. When comparing the methods that use SVM, the distortion is very similar when operated at the same frequency, meaning that the main factor is the modulation frequency, not the control algorithm.

Another advantage of the proposed methods is they actively use the direct axis current to generate

torque throughout the full operation map of the motor, not only in field weakening as the method currently implemented on the car. This is a result of the use of MTPA references which improves efficiency, as it produces a reduction in the current vector modulus, exemplified at ??.

To test the controller's robustness, an error was introduced in the model. The motor parameters were changed by a factor of $\pm 20\%$ without updating the controllers and the step of figure 4.2 was repeated.

- Resistance +20%
- Direct axis inductance +20%
- Quadrature axis inductance -20%
- Permanent Magnet Flux Linkage -20%

This produced some steady state errors on the torque, but the control dynamics were kept, as shown in figure 4.3. Note that the faster rising time is due to the reduced inductance in the quadrature axis, reinforcing the previous statement that this strategy's rising time is only limited by the motor inductances. A small overshoot was also present with the wrong parameters, but its amplitude is very small. Is worth noticing that the error on the parameters did not have a strong effect on the distortion, with the current THD increased only by approximately 0.1%, from 1.05% to 1.14%. Lastly, the load profile defined in

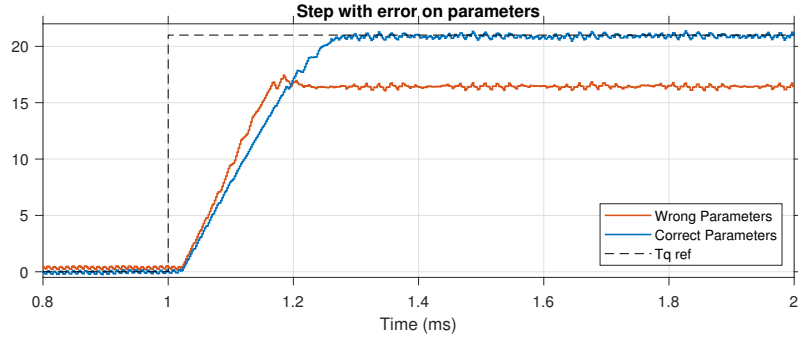


Figure 4.3: Step with error on motor parameters.

Table 4.2: Car load parameters

Car mass	230kg
Pilot mass	70kg
Tire radius	0.24m
Wheel assembly moment of inertia	0.2kgm ²
Gear ratio	15.21
Air density	1.2kg/m ³
Reference car area	1m ²
Drag coefficient	1.59
Rolling resistance coefficient	0.09

section 3.3 was used to simulate a typical acceleration event. The car load parameters are as shown in

table 4.2, and the torque reference was set to reach 26.6kW of delivered power (after inverter and motor efficiency losses). As shown in figure 4.4, the EMPC improved the time from 3.907s to 3.845s (1.6%), reaching also a higher top speed than the currently implemented control method.

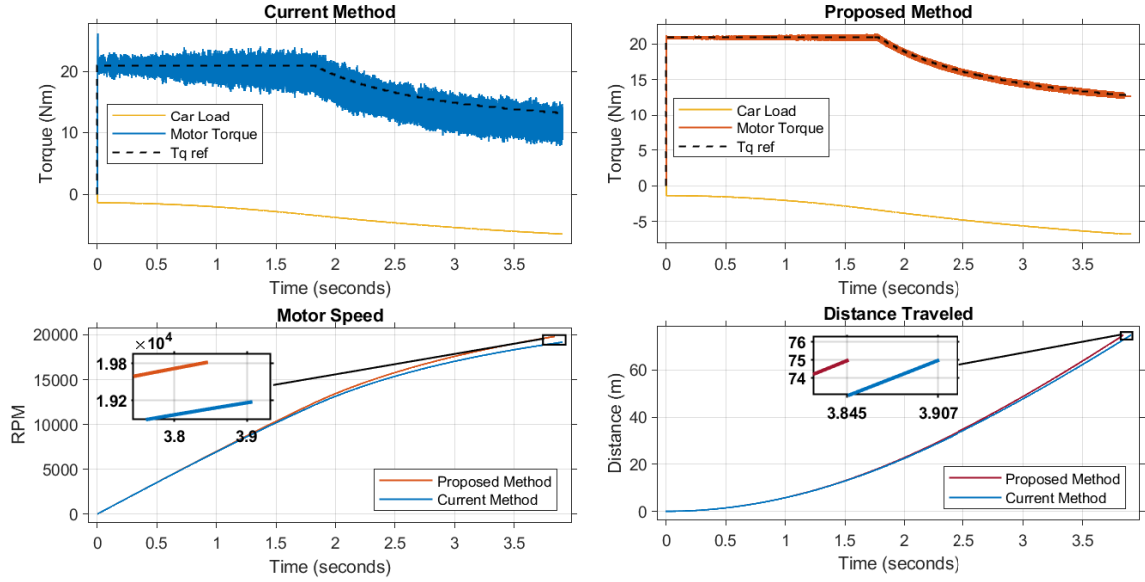


Figure 4.4: Acceleration event comparison.

4.2 Simulation vs Bench Tests

To validate the simulated results, a few bench tests were made. The controller implementation was made using Xilinx Model Composer inside Simulink, compared with the simulation implementation and then generated for a Zybo Z7-20. The hardware used was comprised of the inverter developed on Costa[5], coupled with a current measuring board, developed for this thesis to increase noise immunity. This pairing was supplied with a power supply by Elektro-Automatik (EA-PSI 8360-15 DT) capable of up to 1.5kWh , and the characterized AMK motor was set in a test bench with a Sensor Technology torque transducer (RWT441-EC-PG) and another AMK motor as load. The complete setup is shown in ??.

First, a simple constant torque test was made to evaluate if the model was correctly calculating the generated torque. ?? compares the calculated torque with the ST transducer output, revealing an error smaller than 10%.

Bibliography

- [1] Y. Wang, O. Lucia, Z. Zhang, S. Gao, Y. Guan, and D. Xu. A review of high frequency power converters and related technologies. *IEEE Open Journal of the Industrial Electronics Society*, 1: 247–260, 2020. ISSN 2644-1284. doi: 10.1109/OJIES.2020.3023691.
- [2] P. Karamanakos, E. Liegmann, T. Geyer, and R. Kennel. Model predictive control of power electronic systems: Methods, results, and challenges. *IEEE Open Journal of Industry Applications*, 1:95–114, 2020. ISSN 2644-1241. doi: 10.1109/OJIA.2020.3020184.
- [3] J. W. Palmour. Energy efficient wide bandgap devices. In *2006 IEEE Compound Semiconductor Integrated Circuit Symposium*, pages 4–7, Nov 2006. doi: 10.1109/CSICS.2006.319904.
- [4] J. G. V. V. Sarrico. Design and implementation of a 20kw, 12000rpm permanent magnet synchronous motor (pmsm) for the 1st formula student powertrain. MSc Thesis in Electrical and Computer Engineering, Instituto Superior Técnico, Lisboa, Portugal, June 2017.
- [5] P. M. B. de Sousa Correia da Costa. Compact three-phase sic inverter for the 1st formula student prototype. MSc Thesis in Electrical and Computer Engineering, Instituto Superior Técnico, Lisboa, Portugal, October 2018.
- [6] N. Bianchi, P. G. Carlet, L. Cinti, and L. Ortombina. A review about flux-weakening operating limits and control techniques for synchronous motor drives. *Energies*, 15(5), 2022. ISSN 1996-1073. doi: 10.3390/en15051930. URL <https://www.mdpi.com/1996-1073/15/5/1930>.
- [7] D. Neacsu. Space vector modulation - an introduction. *IECON*, 01 2001.
- [8] S. Vazquez, J. Rodriguez, M. Rivera, L. G. Franquelo, and M. Norambuena. Model predictive control for power converters and drives: Advances and trends. *IEEE Transactions on Industrial Electronics*, 64(2):935–947, Feb 2017. ISSN 1557-9948. doi: 10.1109/TIE.2016.2625238.
- [9] M. Merzoug and F. Naceri. Comparison of field-oriented control and direct torque control for permanent magnet synchronous motor (pmsm). *International Journal of Electrical and Computer Engineering*, 2(9):1797–1802, 2008.
- [10] F. Korkmaz, I. Topaloğlu, M. F. Çakir, and R. Gürbüz. Comparative performance evaluation of foc and dtc controlled pmsm drives. In *4th International Conference on Power Engineering, Energy and Electrical Drives*, pages 705–708, May 2013. doi: 10.1109/PowerEng.2013.6635696.

- [11] R. Souad and H. Zeroug. Comparison between direct torque control and vector control of a permanent magnet synchronous motor drive. In *2008 13th International Power Electronics and Motion Control Conference*, pages 1209–1214, Sep. 2008. doi: 10.1109/EPEPEMC.2008.4635433.
- [12] F. Wang, X. Mei, J. Rodríguez, and R. Kennel. Model predictive control for electrical drive systems—an overview. *CES TRANSACTIONS ON ELECTRICAL MACHINES AND SYSTEMS*, 1(3):219–230, Sep 2017.
- [13] Z. Ma, S. Saeidi, and R. Kennel. Fpga implementation of model predictive control with constant switching frequency for pmsm drives. *IEEE Transactions on Industrial Informatics*, 10(4):2055–2063, Nov 2014.
- [14] *DYNASYN synchronous servo motor DD5-14-10-POW-18600-B5*. AMKmotion GmbH + Co KG, 2018.
- [15] F. S. Germany. Formula student rules 2023 v1.1, 2023. URL https://www.formulastudent.de/fileadmin/user_upload/all/2023/rules/FS-Rules_2023_v1.1.pdf.
- [16] *AMKASYN inverter KW26-S5-FSE-2Q*. AMKmotion GmbH + Co KG, 2022. Version 15.
- [17] E. Gurpinar and A. Castellazzi. Single-phase t-type inverter performance benchmark using si igbts, sic mosfets, and gan hemts. *IEEE Transactions on Power Electronics*, 31(10):7148–7160, Oct 2016. ISSN 1941-0107. doi: 10.1109/TPEL.2015.2506400.
- [18] V. Asadzadeh, A. Dastfan, and A. Darabi. Selective harmonic elimination in direct torque controlled permanent magnet synchronous motor drive. *COMPEL-The international journal for computation and mathematics in electrical and electronic engineering*, 38(1):153–166, 2019.
- [19] Q. An, J. Liu, Z. Peng, L. Sun, and L. Sun. Dual-space vector control of open-end winding permanent magnet synchronous motor drive fed by dual inverter. *IEEE Transactions on Power Electronics*, 31(12):8329–8342, 2016. doi: 10.1109/TPEL.2016.2520999.
- [20] J. Rodríguez, L. Morán, P. Correa, and C. Silva. A vector control technique for medium-voltage multilevel inverters. *IEEE Transactions on Industrial Electronics*, 49(4):882–888, Aug. 2002. ISSN 0278-0046. doi: 10.1109/TIE.2002.801235.
- [21] Microchip. Overmodulation management for field-oriented control of three-phase motors, 2023. URL <https://microchipdeveloper.com/xwiki/bin/view/applications/motors/control-algorithms/3-phase-foc/>.
- [22] F. Briz, A. Diez, M. Degner, and R. Lorenz. Current and flux regulation in field-weakening operation. *Industry Applications, IEEE Transactions on*, 37:42 – 50, 02 2001. doi: 10.1109/28.903125.
- [23] A. Mehrizi-Sani. Advanced modulation techniques for power converters. Master's thesis, University of Manitoba, Winnipeg, Canada, 2007. URL <https://api.semanticscholar.org/CorpusID:58809651>.

- [24] P. Pramod. Circulating current induced electromagnetic torque generation in electric machines with delta windings, 2023.
- [25] G. Marques. *Dinâmica das Máquinas Eléctricas*. April 2002.
- [26] D. Ohm. Dynamic model of pm synchronous motors, 2000. URL <http://www.drvetechinc.com/id16.html>. Drivetech Inc., Technical Article.
- [27] R. De Doncker and D. Novotny. The universal field oriented controller. *IEEE Transactions on Industry Applications*, 30(1):92–100, 1994. doi: 10.1109/28.273626.
- [28] *Sensored Field Oriented Control of 3-Phase Permanent Magnet Synchronous Motors Using TMS320F2837x*. Texas Instruments, 2016.
- [29] H. Le-Huy. Comparison of field-oriented control and direct torque control for induction motor drives. In *Conference Record of the 1999 IEEE Industry Applications Conference. Thirty-Forth IAS Annual Meeting (Cat. No.99CH36370)*, volume 2, pages 1245–1252 vol.2, 1999. doi: 10.1109/IAS.1999.801662.
- [30] T. Matsuo and T. Lipo. Field oriented control of synchronous reluctance machine. In *Proceedings of IEEE Power Electronics Specialist Conference - PESC '93*, pages 425–431, 1993. doi: 10.1109/PESC.1993.471965.
- [31] B. Adhavan, A. Kuppuswamy, G. Jayabaskaran, and V. Jagannathan. Field oriented control of permanent magnet synchronous motor (pmsm) using fuzzy logic controller. In *2011 IEEE Recent Advances in Intelligent Computational Systems*, pages 587–592, 2011. doi: 10.1109/RAICS.2011.6069379.
- [32] G. Buja, D. Casadei, and G. Serra. Dtc-based strategies for induction motor drives. In *Proceedings of the IECON'97 23rd International Conference on Industrial Electronics, Control, and Instrumentation (Cat. No.97CH36066)*, volume 4, pages 1506–1516 vol.4, 1997. doi: 10.1109/IECON.1997.664908.
- [33] A. Nasr, C. Gu, X. Wang, G. Buticchi, S. Bozhko, and C. Gerada. Torque-performance improvement for direct torque-controlled pmsm drives based on duty-ratio regulation. *IEEE Transactions on Power Electronics*, 37(1):749–760, 2022. doi: 10.1109/TPEL.2021.3093344.
- [34] N. El Ouanjli, A. Derouich, e. g. Abdelaziz, S. Motahhir, C. Ali, Y. El Mourabit, and M. Taoussi. Modern improvement techniques of direct torque control for induction motor drives-a review. *Protection and Control of Modern Power Systems*, 4, 05 2019. doi: 10.1186/s41601-019-0125-5.
- [35] L. Zhong, M. Rahman, W. Hu, and K. Lim. Analysis of direct torque control in permanent magnet synchronous motor drives. *IEEE Transactions on Power Electronics*, 12(3):528–536, 1997. doi: 10.1109/63.575680.

- [36] F. Niu, B. Wang, A. S. Babel, K. Li, and E. G. Strangas. Comparative evaluation of direct torque control strategies for permanent magnet synchronous machines. *IEEE Transactions on Power Electronics*, 31(2):1408–1424, 2016. doi: 10.1109/TPEL.2015.2421321.
- [37] S. Vazquez, J. I. Leon, L. G. Franquelo, J. Rodriguez, H. A. Young, A. Marquez, and P. Zanchetta. Model predictive control: A review of its applications in power electronics. *IEEE Industrial Electronics Magazine*, 8(1):16–31, 2014. doi: 10.1109/MIE.2013.2290138.
- [38] X. Sun, J. Cao, G. Lei, Y. Guo, and J. Zhu. A robust deadbeat predictive controller with delay compensation based on composite sliding-mode observer for pmsms. *IEEE Transactions on Power Electronics*, 36(9):10742–10752, 2021. doi: 10.1109/TPEL.2021.3063226.
- [39] R. Errouissi, M. Ouhrouche, W.-H. Chen, and A. M. Trzynadlowski. Robust nonlinear predictive controller for permanent-magnet synchronous motors with an optimized cost function. *IEEE Transactions on Industrial Electronics*, 59(7):2849–2858, 2012. doi: 10.1109/TIE.2011.2157276.
- [40] A. Wijenayake and P. Schmidt. Modeling and analysis of permanent magnet synchronous motor by taking saturation and core loss into account. In *Proceedings of Second International Conference on Power Electronics and Drive Systems*, volume 2, pages 530–534 vol.2, May 1997. doi: 10.1109/PEDS.1997.627416.
- [41] B. Stumberger, G. Stumberger, D. Dolinar, A. Hamler, and M. Trlep. Evaluation of saturation and cross-magnetization effects in interior permanent-magnet synchronous motor. *IEEE Transactions on Industry Applications*, 39(5):1264–1271, Sep. 2003. ISSN 1939-9367. doi: 10.1109/TIA.2003.816538.
- [42] J. D. Barros, J. F. A. Silva, and É. G. A. Jesus. Fast-predictive optimal control of npc multilevel converters. *IEEE Transactions on Industrial Electronics*, 60(2):619–627, 2013. doi: 10.1109/TIE.2012.2206352.

Appendix A

dq0 model with amplitude invariant transformation

Starting with equation (2.3) and replacing the currents and flux for the ones presented in ??:

$$\begin{aligned} \mathbf{u}_{abc} &= \mathbf{R}_{abc} \mathbf{T}_{(\theta_e)}^* \mathbf{i}_{dq0} + \frac{d(\mathbf{T}_{(\theta_e)}^* \psi_{dq0})}{dt} \\ &= \mathbf{R}_{abc} \mathbf{T}_{(\theta_e)}^* \mathbf{i}_{dq0} + \dot{\theta}_e \frac{d\mathbf{T}_{(\theta_e)}^*}{d\theta_e} \psi_{dq0} + \mathbf{T}_{(\theta_e)}^* \frac{d\psi_{dq0}}{dt} \end{aligned}$$

Replacing $\dot{\theta}_e$ with ω_e , and multiplying $\mathbf{T}_{(\theta_e)}^*^{-1}$ to the left results in:

$$\begin{aligned} \mathbf{u}_{dq0} &= \mathbf{R}_{dq0} \mathbf{i}_{dq0} + \mathbf{T}_{(\theta_e)}^*^{-1} \omega_e \frac{d\mathbf{T}_{(\theta_e)}^*}{d\theta_e} \psi_{dq0} + \mathbf{T}_{(\theta_e)}^*^{-1} \mathbf{T}_{(\theta_e)}^* \frac{d\psi_{dq0}}{dt} \\ \mathbf{u}_{dq0} &= \mathbf{R}_{dq0} \mathbf{i}_{dq0} + \omega_e \mathbf{T}_{(\theta_e)}^*^{-1} \frac{d\mathbf{T}_{(\theta_e)}^*}{d\theta_e} \psi_{dq0} + \frac{d\psi_{dq0}}{dt} \end{aligned}$$

Lastly, calculate the derivative of the transformation:

$$\begin{aligned} \mathbf{T}_{(\theta_e)}^*^{-1} \frac{d\mathbf{T}_{(\theta_e)}^*}{d\theta_e} &= \frac{2}{3} \begin{bmatrix} \cos(\theta_e) & \cos(\theta_e - \frac{2\pi}{3}) & \cos(\theta_e - \frac{4\pi}{3}) \\ -\sin(\theta_e) & -\sin(\theta_e - \frac{2\pi}{3}) & -\sin(\theta_e - \frac{4\pi}{3}) \\ \frac{1}{2} & \frac{1}{2} & \frac{1}{2} \end{bmatrix} \begin{bmatrix} -\sin(\theta_e) & -\cos(\theta_e) & 0 \\ -\sin(\theta_e - \frac{2\pi}{3}) & -\cos(\theta_e - \frac{2\pi}{3}) & 0 \\ -\sin(\theta_e - \frac{4\pi}{3}) & -\cos(\theta_e - \frac{4\pi}{3}) & 0 \end{bmatrix} \\ \mathbf{T}_{(\theta_e)}^*^{-1} \frac{d\mathbf{T}_{(\theta_e)}^*}{d\theta_e} &= \begin{bmatrix} 0 & -1 & 0 \\ 1 & 0 & 0 \\ 0 & 0 & 0 \end{bmatrix} \end{aligned}$$

Thus, the PMSM model in the dq0 frame using amplitude invariant transformation is presented in equation (A.1). This result is the same as equation (2.11), but the currents, voltages, and fluxes are scaled

by a factor of $\sqrt{\frac{3}{2}}$ in the direct and quadrature axis, but in the zero axis some results may vary.

$$\mathbf{u}_{dq0} = \mathbf{R}_{dq0} \mathbf{i}_{dq0} + \omega_e \begin{bmatrix} 0 & -1 & 0 \\ 1 & 0 & 0 \\ 0 & 0 & 0 \end{bmatrix} \boldsymbol{\psi}_{dq0} + \frac{d\boldsymbol{\psi}_{dq0}}{dt} \quad (\text{A.1})$$

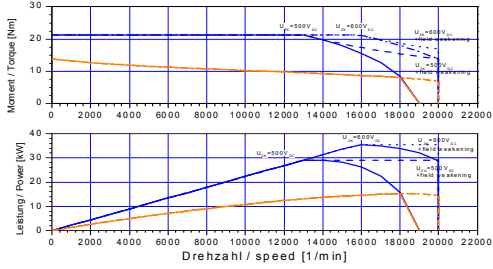
Appendix B

Technical Datasheets

B.1 AMK Motor Datasheet

Motor-Datenblatt motor data sheet

AMK

Bezeichnung/name	<u>DD5-14-10-POW</u> - 18600-B5	- Formula Student	Datum/date:	27.11.2018	
Teile-Nr./part number	A2370DD	Zeichn.-Nr./drawing no.:12703-01260			
Motorbeschreibung motor description:					
Motorprinzip/motor principle: Kühlart/cooling type: Bauform/mounting type: Schutzart/degree of protection: Isolierklasse/insulation class:					
Leistungsdaten performance data:					
Betriebsart/duty type: Dauerstillstandsmoment/continuous Stall Torque "Mo": Maximales Moment/maximum torque "Mmax": Bemessungsmoment/rated torque "Mn" (ID32771): Bemessungsleistung/rated power "Pn": Bemessungsdrehzahl/rated speed "Nn" (ID32772): Theo. Leerlaufdrehzahl/theor. no-load-speed "No":					
Motorkennlinien performance - characteristics:					
 <p>Kennlinie kann die maximal zulässige Drehzahl übersteigen! / Characteristic may exceed mechanical speed limit of motor</p>					
Elektrische Daten electrical data: Nennspannung/rated voltage "Un" (ID32768): Nennstrom/rated current "In" (ID111): Dauerstillsstrom/cont. stall current "Io" (ID34096): Maximalstrom/maximum current "Imax" (ID109): Maximale Dauer für/duration for "Imax" (ID34168): Drehmomentkonstante/torque constant "kT": Spannungskonstante/voltage constant "ke" (ID 34234): Schaltung/connection type: Polzahl/number of poles "2p" (ID32775): Klemmenwiderstand/terminal resistance "Rtt" (ID34164): Klemmeninduktivität/terminal inductance "Ltt" (ID34167): Querachseninduktivität/quadrature axis inductance "Lq" (ID34046): Hauptsachseninduktivität/direct axis inductance "Ld" (ID34045): Magn.-Ström/magn. current "Im" (ID32769): Magn.-Ström/magn. current "Im1" (ID32770): Rotorzeitkonstante/rotor time constant "Tr" (ID32774): Reglereinstellungen controller settings: Stromregler current controller: Verstärkung q-Achse/gain q-axis "Kpq" (ID34151): Verstärkung d-Achse/gain d-axis "Kpd" (ID34152): Nachstellzeitkonstante/time constant "Tnq" (ID34050): Nachstellzeitkonstante/time constant "Tnd" (ID34052): Adaption Verstärkung/adaption gain "Kpq2" (ID 34179) Adaption Nachstellzeit/adaption time constant "Tnq2" (ID 34180) Untere Anpaßschwelle/lower adaption limit "Iua" (ID34177): Obere Anpaßschwelle/upper adaption limit "Ioa" (ID34178): Drehzahlregler speed controller (default for plain motor): Verstärkung/gain "Kp_n" (ID100): Nachstellzeitkonstante/time constant "Tn_n" (ID101): Spannungsregler voltage controller: Spannungsregler/voltage controller "Kp" (ID34148): Spannungsregler/voltage controller "Tn" (ID34149): Spannungsüberhöhung "dU" (ID34235): Systemwiderstand "Rs" (ID34233): 					

Für dieses Dokument und die darin enthaltenen Angaben behalten wir uns alle Rechte und technische Änderungen vor.
All rights reserved for this document and all information included. Technical modifications reserved
(c) AMK Antriebs- und Steuerungstechnik GmbH Co. KG

Motor-Datenblatt motor data sheet

AMK

Bezeichnung/name	<u>DD5-14-10-POW</u> - 18600-B5	- Formula Student	Datum/date:	27.11.2018	
Teile-Nr./part numbe	A2370DD	Zeichn.-Nr./drawing no.: 12703-01260			
Mechanische Daten mechanical data:					
Gesamtmasse/motor mass "m": Motorträgheitsmoment/inertia "J": Mech. zul. Drehzahl/mech. speed limit "Nmax": Rundlauf/run out (DIN 42955): Wuchtgüte/balancing quality: Passfeder/shaft key:					
Bremsendaten brake data:					
Typ/type: Bremsmoment/brake torque: Bremsenstrom/brake current: Bremsenspannung/brake voltage: Spannungsart/voltage type: Einfallzeit/engage time "Te": max. Bremsenergie/max. braking energy: einmalig/single engagement: Lebenslang/lifetime:					
Lüfterdaten fan data:					
AMK-TNr./AMK part number: Lüfterspannung/fan voltage: Strom/current: Frequenz/frequency:					
Wicklungsschutz thermistor:					
Typ/type (ID34166): KTY84 Ansprechtemp./operation temp: - °C Widerstand/resistance (25°C) <=: 629 Ω					
Geberdaten position encoder data:					
AMK-TNr./AMK part number: 108072 Typ/type: P Impulszahl/number of pulses: 262144					
Bemerkungen remarks:					
automatisch erstellt, Geber 18 Bit, Sonderparameter FSE Daten nur gültig mit entsprechender Wasserkühlung					

* Typenschildbezeichnung unterstrichen; bitte bei Rückfragen immer angeben / Nameplate data underlined; please state with every inquiry

Ersteller/created by: SMM Änderungsstand Mechanik/revision motor-mechanics: 0.00 Änderungsdatum/motor revision motor date 26.10.2016

Für dieses Dokument und die darin enthaltenen Angaben behalten wir uns alle Rechte und technische Änderungen vor.
All rights reserved for this document and all information included. Technical modifications reserved
(c) AMK Antriebs- und Steuerungstechnik GmbH Co. KG

4 Technical data

4.1 Technical data – inverter

	Terminal / strand	KW26-S5-FSE-4Q (2WD inverter) (data per inverter)
Rated input voltage HV+, HV- power supply	HV+, HV-	540 VDC
Input voltage range		250 VDC - 720 VDC
Input current Power supply for HV = 540 VDC		48 A
Intermediate circuit capacity		75 µF
Supply voltage for logic supply LV	X08 (X09)	24 VDC ±15%, The 0 V potential must be connected to the vehicle ground (vehicle chassis).
Input current for logic supply LV		≤ 500 mA
Capacity at input of internal switched-mode power supply		1,500 µF
Efficiency		Approx. 98%
Ground		Vehicle ground (vehicle chassis) or ground strap Switching GND for logic voltage is internally connected to the frame of the inverter
Control method Switching frequency		PWM 8 kHz
Output frequency¹⁾	U, V, W	0 - 1200 Hz
Output voltage (HV = 540 VDC)		350 VAC (sinusoidal output current)
Output voltage range (HV = 250 - 720 VDC)		160 - 490 VAC
Rated output power		26 KVA
Rated output current I_N		43 A
Peak output current I_{max}		107 A
Max. duration of peak output current I_{max} • Output frequency $f_{OUT} > 1$ Hz		10 s
Max. duration of peak output current I_{max} • Output frequency $f_{OUT} \leq 1$ Hz		1 s
Temperature sensor evaluation	X12	KTY e.g., KTY84-130
Protective / monitoring function		Short-circuit / ground fault, intermediate circuit overvoltage, excess temperature at motor / heat sink, current overload as per I^2t
Galvanic isolation voltage between HV and LV		2200 VDC
Cooling		Liquid cooling
Flow rate		1.5 bar / 10 l/min
Max. cold plate and ambient temperature		40 °C
Protection class		IP 00

	Terminal / strand	KW26-S5-FSE-4Q (2WD inverter) (data per inverter)
Dimensions (2WD inverter)	Approx. 339 mm length, approx. 183 mm width, approx. 131 mm height	
Weight for 2WD inverter including heat sink	Approx. 6,3 kg	

1) Speed setpoint values are limited to 30000 rpm

4.2 Technical data – motor

Please refer to the motor data sheet (see: Motor_data_sheet_A2370DD_DD5) for the technical data for the motor.



When the system is started up for the first time, the motor parameters are automatically transferred from the encoder database to the inverter.

The function is not performed if the motor parameters have already been entered manually. The AIPEX PRO's 'Initial program loading' (PW: 500591) function in direct mode allows the factory settings from AMK to be restored.

Prerequisite for the automatic transfer of the data from the encoder database:

- Encoder cable connected
- Motor parameters have not already been changed manually
- The data has been stored in the encoder at the factory